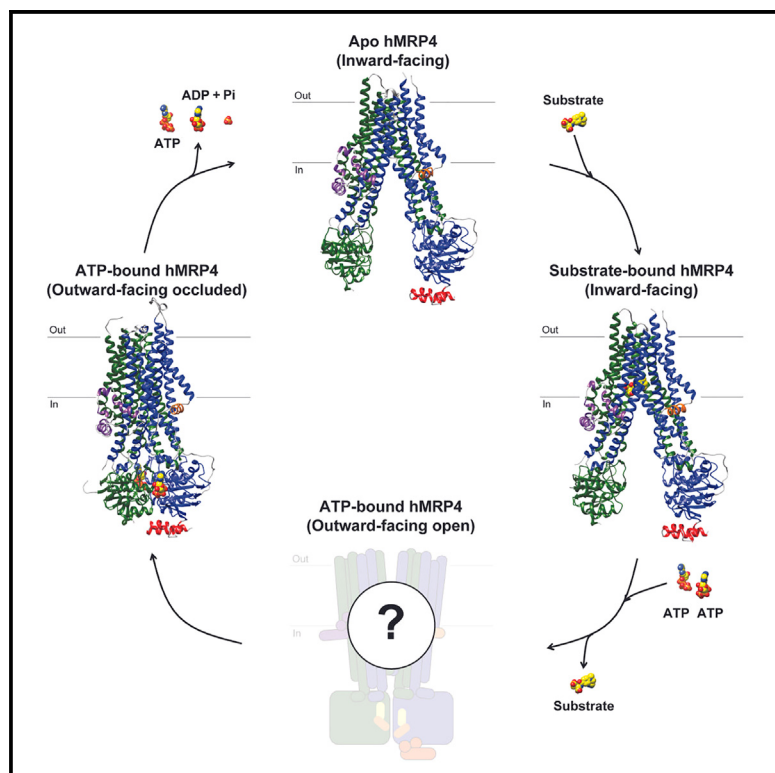


Structure

Structural and mechanistic basis of substrate transport by the multidrug transporter MRP4

Graphical abstract



Authors

Magnus Bloch, Isha Raj, Tillmann Pape, Nicholas M.I. Taylor

Correspondence

nicholas.taylor@cpr.ku.dk

In brief

Bloch et al. used cryo-EM to determine multiple structures of lipid bilayer-embedded human MRP4. Functional and mutational studies were used to validate the structural models of human MRP4, which provide key insights into the structural and mechanistic basis of substrate transport by this important multidrug transporter.

Highlights

- Multiple structures of bilayer-embedded human MRP4 were determined using cryo-EM
- Human MRP4 adopts an outward-facing occluded conformation during transport cycle
- Bipartite binding pocket allows coordination of chemically diverse substrates
- Biological activity of human MRP4 is modulated by both substrates and bound lipids



Article

Structural and mechanistic basis of substrate transport by the multidrug transporter MRP4

Magnus Bloch,¹ Isha Raj,¹ Tillmann Pape,^{2,3} and Nicholas M.I. Taylor^{1,4,*}¹Structural Biology of Molecular Machines Group, Protein Structure & Function Program, Novo Nordisk Foundation Center for Protein Research, Faculty of Health and Medical Sciences, University of Copenhagen, Blegdamsvej 3B, 2200 Copenhagen, Denmark²Structural Molecular Biology Group, Protein Structure & Function Program, Novo Nordisk Foundation Center for Protein Research, Faculty of Health and Medical Sciences, University of Copenhagen, Blegdamsvej 3B, 2200 Copenhagen, Denmark³Core Facility for Integrated Microscopy (CFIM), Faculty of Health and Medical Sciences, University of Copenhagen, Nørre Allé 20, 2200 Copenhagen, Denmark⁴Lead contact*Correspondence: nicholas.taylor@cpr.ku.dk<https://doi.org/10.1016/j.str.2023.08.014>

SUMMARY

Multidrug resistance-associated protein 4 (MRP4) is an ATP-binding cassette (ABC) transporter expressed at multiple tissue barriers where it actively extrudes a wide variety of drug compounds. Overexpression of MRP4 provides resistance to clinically used antineoplastic agents, making it a highly attractive therapeutic target for countering multidrug resistance.

Here, we report cryo-EM structures of multiple physiologically relevant states of lipid bilayer-embedded human MRP4, including complexes between MRP4 and two widely used chemotherapeutic agents and a complex between MRP4 and its native substrate. The structures display clear similarities and distinct differences in the coordination of these chemically diverse substrates and, in combination with functional and mutational analysis, reveal molecular details of the transport mechanism. Our study provides key insights into the unusually broad substrate specificity of MRP4 and constitutes an important contribution toward a general understanding of multidrug transporters.

INTRODUCTION

ATP-binding cassette (ABC) transporters are integral membrane proteins that utilize binding and hydrolysis of ATP for moving molecules across cellular membranes. The human genome encodes 48 different ABC transporters that can be divided into seven subfamilies (A–G) based on sequence homology and domain arrangement.¹ Belonging to the category of type IV transporters,² subfamily C features a group of efflux transporters characterized by unusually broad substrate specificities³ known as multidrug resistance-associated proteins (MRPs).

Uniquely among the MRPs, MRP4 is found in both apical and basolateral membranes of crucial tissue barriers such as the blood-brain barrier and blood-cerebrospinal fluid barrier,^{4,5} where it exports a wide variety of organic anions,⁶ including many chemotherapeutic agents.^{3,7} In addition, MRP4 has been found to be overexpressed in cancer cells, where its efflux activity contributes to multidrug resistance (MDR): Expression of MRP4 is increased in neuroblastoma,⁸ hepatocellular carcinoma,⁹ lung cancer,¹⁰ breast cancer,¹¹ and prostate cancer.¹² MRP4 overexpression has been found to provide cells with resistance to a wide range of clinically used antineoplastic agents such as thiopurines,^{13,14} antifolates,¹⁵ and camptothecins^{5,8,16} as well as enhance the extrusion of antiviral^{17–19} and antibiotic^{20,21} compounds.

The extensive tissue distribution and pronounced substrate promiscuity of MRP4 and other MRPs make them important factors to consider when attempting drug delivery.^{22,23} Additionally, their MDR-inducing overexpression makes them attractive therapeutic targets. However, a detailed understanding of the structural and mechanistic basis of their substrate recognition and translocation is currently lacking, preventing the development of effective modulators that specifically target the efflux activity of these promiscuous drug transporters.

While recent structural studies have yielded high-resolution molecular structures of multiple members of the ABCB and ABCG subfamilies,^{24–41} the MRPs of the ABCC subfamily remain relatively understudied. Recently, structures of bovine MRP1 were determined,^{42–44} but structures of human MRPs in well-defined lipid systems mimicking biological conditions, have so far not been resolved, precluding a deeper understanding of the mechanism of action of this physiologically and therapeutically important group of proteins.

In this study, we used cryo-electron microscopy (cryo-EM) to determine the structure of lipid bilayer-embedded human MRP4 and investigate its substrate coordination and translocation. Functional and mutational studies were used to validate the structural models of MRP4, which provide key insights into the structural and mechanistic basis of its substrate transport.



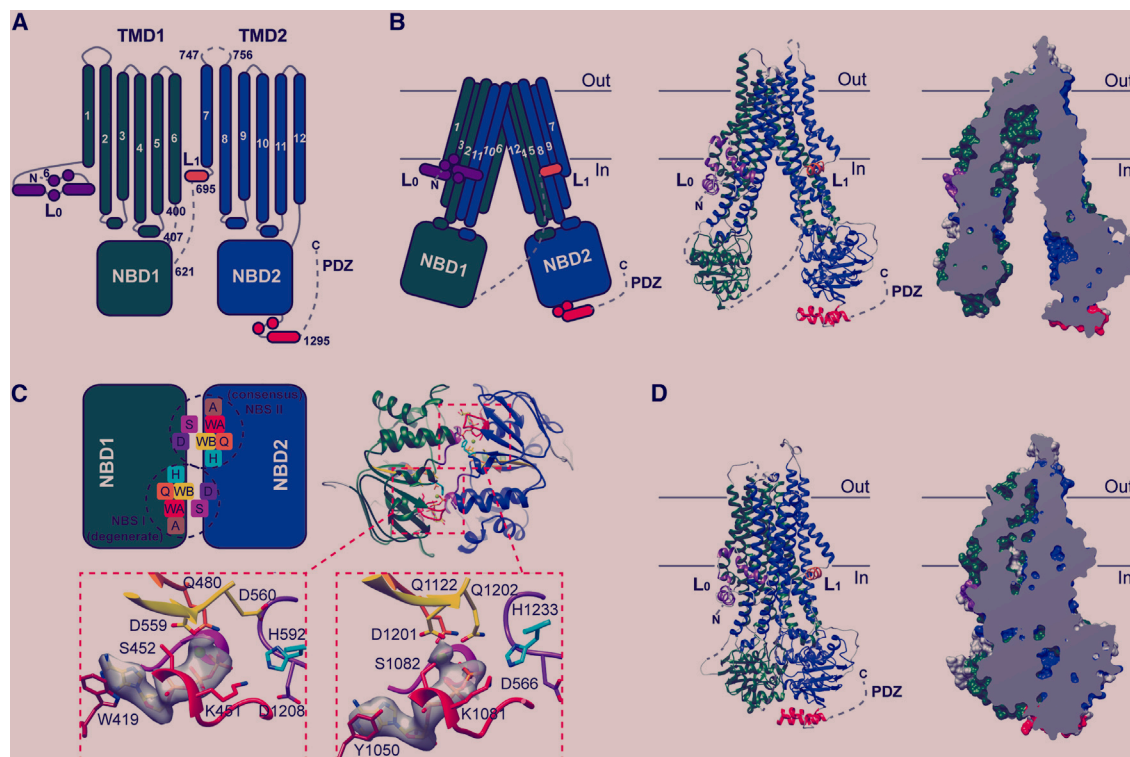


Figure 1. The molecular architecture of human MRP4

(A) Cartoon representation of structural elements of hMRP4. Dashed lines represent elements (sequence position indicated with numbers) for which model building was not possible. Transmembrane helices are numbered from N-terminus (N) to C-terminus (C). L₀ = Lasso motif, L₁ = C-terminal elbow helix, PDZ = PDZ-binding motif.

(B) Representations of the hMRP4 IF conformation (viewed from within the membrane plane, indicated with gray lines: Out = extracellular side, In = intracellular side). Left: Cartoon representation of the hMRP4 IF model. Middle: Ribbon representation of the hMRP4 IF model. Right: Slabbed surface representation of the hMRP4 IF model.

(C) Representations of the hMRP4 OF conformation (viewed from the intracellular side). Top: Cartoon and ribbon representations of the two composite nucleotide-binding sites (NBS I and II) and their ABC motifs (colored boxes): A (brown) = A-loop, WA (red) = Walker A, Q (orange) = Q-loop, WB (yellow) = Walker B, H (cyan) = H-switch, D and S (purple) = D loop and Signature motif. Bottom: Zoomed-in view of isolated ABC motifs. Gray surface represents map density (contoured at $\sigma = 0.70$) within 2.0 Å of the molecular models of bound ATP molecules (shown as sticks) coordinated by Mg²⁺-ions (green spheres).

(D) Left: Ribbon representation of the hMRP4 OF model. Right: Slabbed surface representation of the hMRP4 OF model.

RESULTS

The molecular architecture of bilayer-embedded MRP4

MRP4 displays a canonical ABC transporter architecture (Figure 1A) featuring two globular nucleotide-binding domains (NBDs) and two helical transmembrane domains (TMDs). The six transmembrane helices of each TMD connect via extracellular loops and intracellular-coupling helices, and each NBD harbors a complete set of ABC sequence elements (the ATP-binding cassette). In combination, the two sets make up two composite nucleotide-binding sites: a degenerate site, featuring noncanonical sequence elements, and a consensus site, which is strictly canonical and capable of catalyzing ATP hydrolysis.

Like all other type IV exporters,² MRP4 features elbow helices immediately preceding the TMDs. The N-terminal elbow helix forms part of an ABCC-specific lasso motif (L₀) and the C-terminal elbow helix (L₁) connects indirectly to NBD1 via an extended linker. Among the MRPs, MRP4 features an unusually long C-terminal tail that contains a PDZ-binding motif (PDZ) at the C-terminus.⁴²

Cryo-EM was used to determine the three-dimensional molecular structure of MRP4. To mimic biological conditions, purified MRP4 was reconstituted in the bilayer environment of lipid nanodiscs prior to structural studies.

The substrate-accepting inward-facing conformation

We were able to reconstitute MRP4 into nanodiscs prepared using brain polar lipid (BPL) extract supplemented with the cholesterol analog, cholesteryl hemisuccinate (CHS) (Figure S1A). From this sample of BPL+CHS nanodisc complexes, we could reconstruct a map corresponding to a distinct inward-facing (IF) state (Figure S2).

In this conformation (Figure 1B), the overall domain arrangement of MRP4 is similar to that observed for other type IV exporters²: Two transmembrane helices from each TMD domain-swap into the other TMD forming two helical bundles, with each bundle interacting directly with one NBD via its associated coupling helices. Characteristic of the IF conformation, the extracellular and transmembrane parts of the TMDs form close contacts, while the intracellular parts and the NBDs are completely separated.

The TMDs form a transmembrane cavity, which is firmly sealed at the outer bilayer leaflet and opens toward the intracellular side. The elbow helices are situated at the cytoplasmic interface of the inner leaflet in an orientation parallel to the lipid bilayer, and L_0 extends toward L_1 on one side of the transporter. The initial stretch of the C-terminal tail adopts a distinct helical fold, while the structure of the extreme C-terminal region (including the PDZ-binding motif) and the linker (residues 621–695) remain unresolved.

The cryo-EM map of the BPL+CHS nanodisc complex features multiple distinct densities corresponding to tightly bound molecules of either cholesterol or CHS (Figure S7). To investigate the effects of these annular lipids, cryo-EM was applied to wild-type human MRP4 reconstituted in nanodiscs made using synthetic POPC (Figure S1B). Although the overall shape of the two reconstructions was the same (Figures S8A and S8B), the quality of the map obtained from the sample of POPC nanodisc complexes did not allow for detailed model building.

The occluded outward-facing conformation

Extensive efforts at resolving additional globally distinct conformations of wild-type human MRP4 reconstituted in BPL+CHS nanodiscs were unsuccessful. In an attempt to promote the population of alternative conformational states, the catalytic glutamate (E1202) of the consensus site Walker B motif was mutated to a glutamine. This mutation effectively eliminates hydrolytic activity without affecting ATP binding⁴³ and has previously been successfully employed to obtain structures of NBD-dimerized intermediates of other ABC transporters.^{24,27,35,44} However, alternative conformations could still not be distinctly resolved using cryo-EM on samples of E1202Q (EQ) MRP4 in BPL+CHS nanodiscs, and it was not until EQ MRP4 was reconstituted in POPC nanodiscs (Figure S1C) that a map clearly corresponding to a different conformation was obtained (Figure S3).

In this conformation, the NBDs are closely associated (Figure 1C), completing the degenerate and consensus nucleotide-binding sites at their interface, which both harbor an Mg^{2+} -coordinated ATP molecule. The intracellular parts of the transmembrane bundles are in close contact (Figure 1D), shutting the intracellular opening of the collapsed transmembrane cavity, which also in this conformation is sealed off toward the extracellular side. Consequently, the resolved structure represents an outward-facing (OF) occluded state.

As opposed to the map corresponding to wild-type human MRP4 in BPL+CHS nanodiscs (Figure S2), the map of EQ MRP4 in POPC nanodiscs (Figure S3) does not feature any distinct densities corresponding to annular lipids, despite the maps being of similar resolution.

MRP4 is differentially modulated by chemically distinct substrates

To investigate the functional significance of the observed annular lipids, ATPase activities of both types of nanodisc complexes (BPL+CHS and POPC) were quantified (Figure 2) using two assays (ADP-Glo and PiColorLock). Both ATPase activity assays showed that wild-type MRP4 exhibits a markedly (~ 4 -fold) higher basal activity when it is reconstituted in BPL+CHS nanodiscs compared to when it is reconstituted in POPC nanodiscs. To account for potential copurification of other ATP-decompos-

ing factors, ATPase activity of equivalent preparations (Figure S1C) of EQ MRP4 and K1081M (KM) MRP4 (the latter carrying a mutation in the consensus site Walker A motif that interferes with ATP hydrolysis⁴⁵) was also investigated (Figure S1D). Neither of these control preparations exhibited detectable ATPase activity.

The same two assays were used to investigate how MRP4 ATPase activity is affected by the presence of substrates. The endogenous substrate, prostaglandin E2 (PGE2), strongly stimulated basal ATPase activity of both types of nanodisc complexes, while the exogenous substrate methotrexate (MTX) only moderately stimulated basal activity. Another exogenous substrate, topotecan (TPT), was found to decrease the observed ATPase activity below basal levels for both nanodisc complexes. Therefore, all three substrates appear to interact with functional wild-type protein, although they modulate ATPase activity in different ways.

The structural basis of MRP4 substrate promiscuity

To investigate the structural basis of the interaction between MRP4 and these substrates, cryo-EM was applied to samples of WT MRP4 in POPC nanodiscs incubated with either MTX, TPT, or PGE2 (see STAR Methods for details). All the resulting maps (Figures S4–S6) featured distinct densities inside the transmembrane cavity (Figures S9A–S9C) into which molecular models of the respective substrates could be fitted. Consequently, as observed for other ABC transporters, the inward-facing transmembrane cavity appears to constitute a substrate-binding pocket (Figure 3).

In all three cryo-EM maps, density corresponding to the central ring structures of all three substrates is more distinct than that corresponding to distal segments (Figure S10). The distal section of the diaminopteridin moiety of the modeled MTX molecule is not as well-resolved as the central benzoyl group (Figure S10A), and the map density of the dimethylamino group of the modeled TPT molecule is not as distinct as that of the polycyclic core (Figure S10B). While the modeled conformation of PGE2 (Figure S10C) would be capable of engaging in specific-directed interactions with surrounding residues (Figures 3 and S9C), the density corresponding to the flexible hept-5-enoic acid moiety is relatively indistinct, suggesting potential coexistence of an alternative binding pose (Figure S10D).

All three substrates sit in close proximity to the central W995 residue (Figures S9A–S9C and 3), which is located at the interface between a predominantly hydrophilic, positively charged half and a predominantly hydrophobic half of the substrate-binding pocket, referred to as the P-pocket and the H-pocket, respectively.⁴⁶ The flat and polycyclic TPT can readily engage in π - π stacking interactions with the indole ring of W995, while the flexible, two-tailed PGE2 appears to engage in H-bonds and salt bridges with residues of the P-pocket via its carboxyl group. The characteristically kinked aromatic moiety of MTX appears to be capable of forming extensive van der Waals (vdW) and π - π stacking interactions with residues of the H-pocket, while the negatively charged carboxyl moiety of the molecule may engage with residues of the P-pocket via long-range electrostatic interactions (Figure 3).

Careful examination of the map of IF hMRP4 (no substrate added) (Figure S2) at low-contour levels, revealed a slight

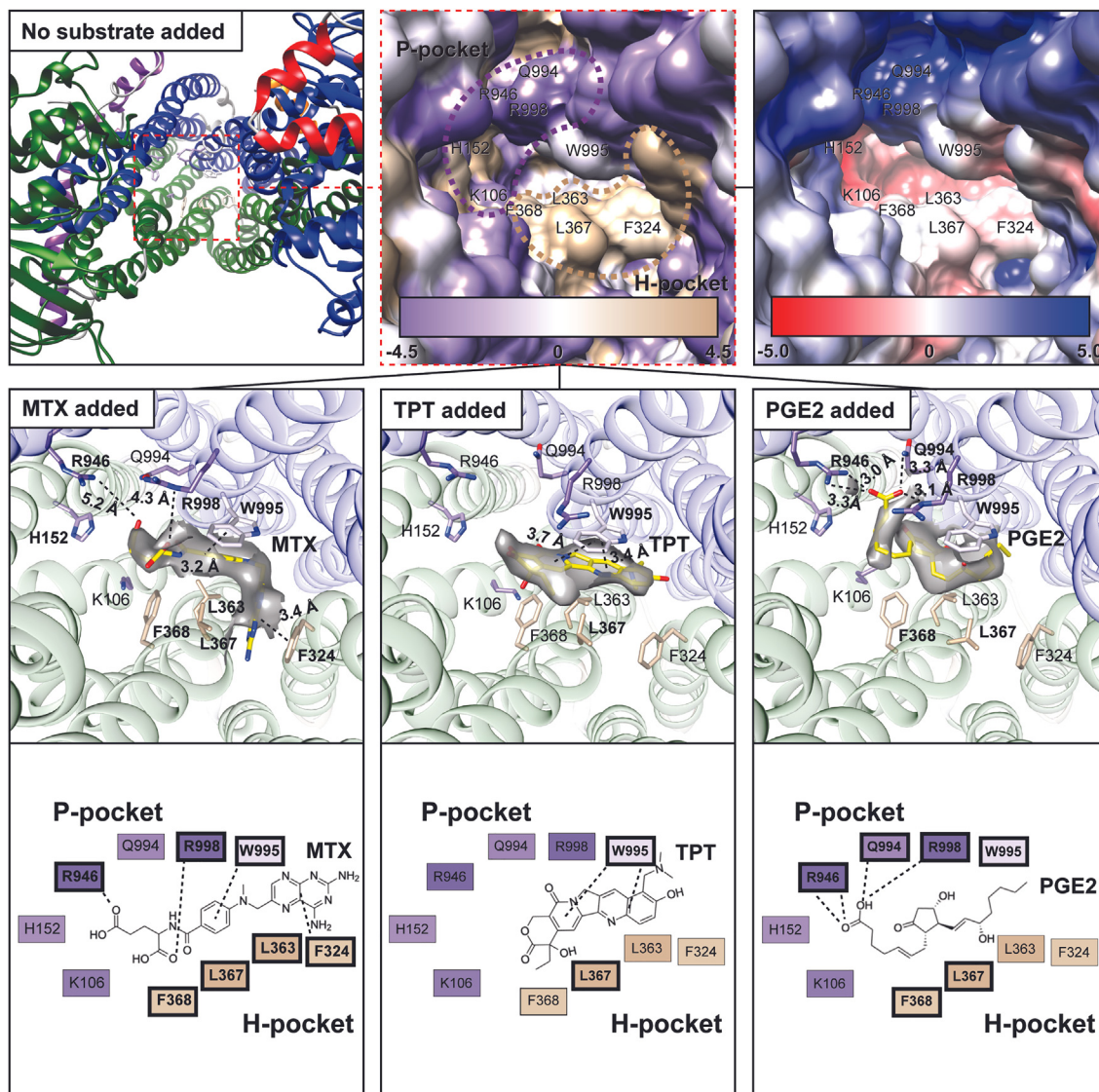


Figure 3. Characterization of the MRP4 substrate-binding pocket and its substrate coordination

Top left: Ribbon representation of the molecular model of IF hMRP4 (no substrate added). Top middle: Zoomed in surface representation of the same model with residue surfaces colored according to the Kyte-Doolittle hydrophobicity scale.⁷² Scale: purple, negative (−4.5); tan, positive (4.5). Top right: The same surface representation colored according to electrostatic properties. Scale: red, negative (−5.0 kT/e); blue, positive (5.0 kT/e). Middle row: Ribbon representations of molecular models of IF hMRP4 built into the maps obtained from samples to which the indicated substrates have been added (see STAR Methods for details). Key residues and models of bound substrate are shown as sticks, and potential directed interactions are indicated with punctured lines (distance between interacting centers indicated in Å). Gray surface represents map density within 2.0 Å of the molecular models of MTX, TPT, and PGE2 (contoured at $\sigma = 0.40, 0.27,$ and 0.20 respectively). Residues whose side chains potentially engage directly with bound substrate are highlighted in bold. Bottom row: 2D representations (based on information presented in Figure S9 and the representations above) of substrate coordination with potentially contacting residues outlined in bold and directed interactions indicated with punctured lines.

Western blotting was used to assess expression levels of recombinant MRP4 in all investigated cell lines (Figure 4D). While a complete lack of recombinant MRP4 expression was observed for the parental cell line (NEG), all other cell lines appear to have similar expression levels of their respective MRP4 variant, except for the cell lines overexpressing the H152A and K106A variants. Interestingly, while expression of these variants was not as clearly detected by Western blot analysis, the cell lines nonetheless displayed R phenotypes (Figures 4C and S11), indi-

cating that they have the same MTX efflux capability as the cell line overexpressing wild-type hMRP4.

DISCUSSION

Modulation by annular lipids and substrates

Multiple recent studies have demonstrated the profound effect the reconstitution environment can have on ABC transporter structure and function,^{47–50} underscoring the importance of

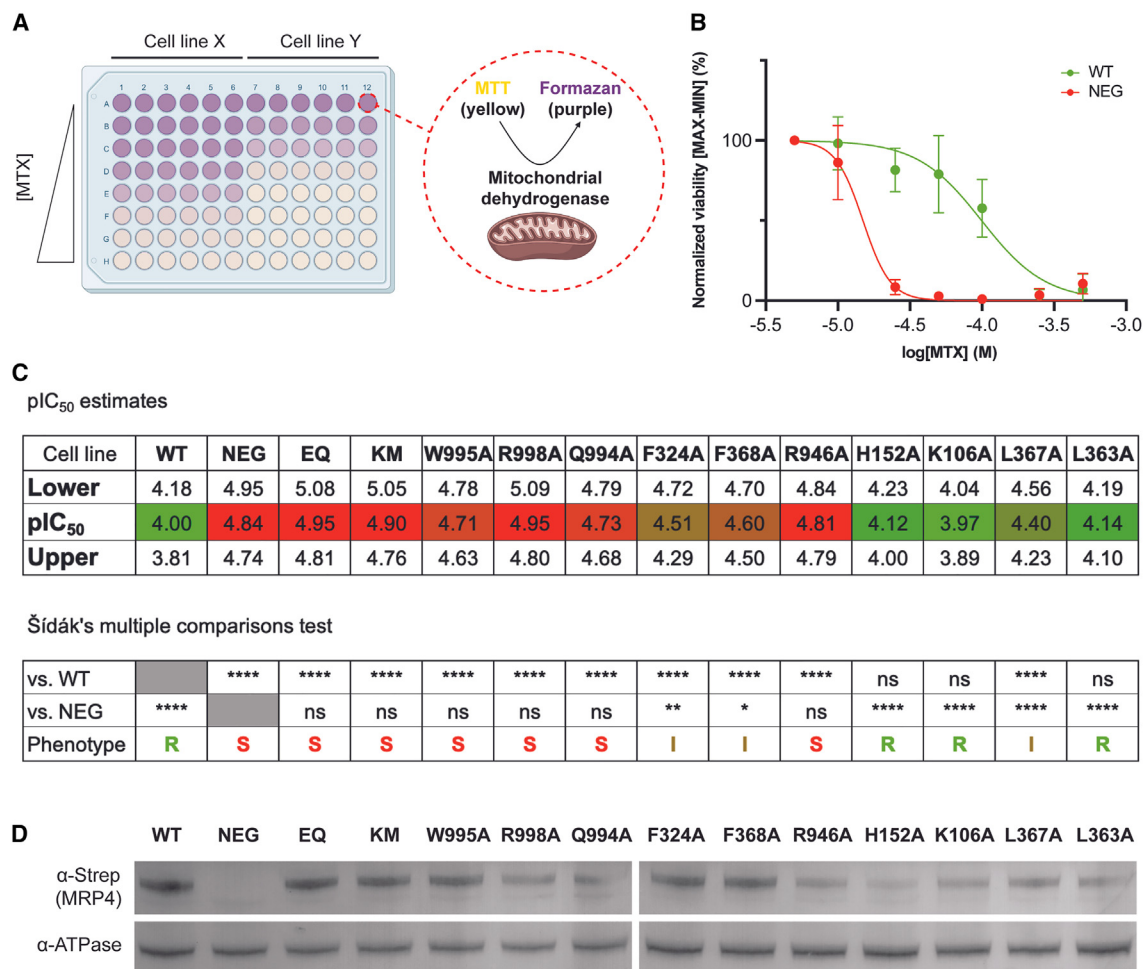


Figure 4. Mutational analysis of the MRP4 substrate translocation mechanism

(A) Cartoon representation of the cellular drug susceptibility assay used for mutational analysis. In principle, the mitochondria of metabolically active cells convert soluble MTT (yellow color) to insoluble Formazan (purple color) with development of purple color thus being proportional to the number of metabolically active cells (and used as a measure of cell viability).

(B) Illustrative plot of normalized cell viability vs. MTX concentration (on log₁₀ scale) for the cell line overexpressing wild-type hMRP4 (WT) and the parental cell line (NEG). For this plot, normalized cell viability was calculated by normalizing to viability at lowest non-zero [MTX] (5 μM) and then normalizing to the MAX-MIN range. Each data point represents the average of nine independent experiments (each with six technical replicates), the error bars represent standard deviations, and the curves represent fits of sigmoidal dose-response models to the data.

(C) Table displaying values of mean pIC₅₀ (p = -log₁₀) for individual cell lines as estimated by the cellular drug susceptibility assay, including lower and upper 95% confidence intervals for the estimates (all fits from which these estimates are obtained are shown in Figure S11). The mean pIC₅₀ values are color-coded from red (equivalent to pIC₅₀(NEG) = 4.84) to green (equivalent to pIC₅₀(WT) = 4.00). The lower table displays the results of a Šidák's multiple comparisons test and the corresponding phenotypic interpretation (see Quantification and Statistical Analysis).

(D) Western blots of extracts from equivalent preparations of individual cell lines. Top section: Detection of recombinant hMRP4. Bottom section: Detection of endogenous sodium potassium ATPase (loading control).

studying these transporters under conditions mimicking their native membrane environment.

In this study, single-particle cryo-EM of human MRP4 in lipid nanodiscs revealed that the TMDs of MRP4 can form specific interactions with lipid molecules that appear to affect conformational dynamics: BPL+CHS nanodisc complexes of wild-type MRP4, in which ordered lipids associate with the transporter, exhibit markedly higher basal catalytic activity than POPC nanodisc complexes, and while the wild-type transporter preferentially assumes IF states in both lipid environments (regardless of substrate addition), the relatively low

resolution of the cryo-EM reconstruction obtained from the sample of POPC nanodisc complex without added substrate may indicate a high-inherent transporter flexibility compared to the BPL+CHS complex. Furthermore, the NBD-dimerized (OF) state of EQ MRP4 could only be resolved in POPC nanodiscs, while it remained elusive for equivalent samples of EQ MRP4 in BPL+CHS nanodiscs. Ordered lipids have also been found in recently resolved structures of multiple other ABC transporters,^{25,37,44} making it increasingly clear that many, if not all, ABC transporters form specific interactions with lipids.

However, it is not only the lipid composition of the membrane bilayer that can strongly affect conformational dynamics but also the presence of substrates and other modulators.

As demonstrated in this study, while presence of substrate modulates the ATPase activity of nanodisc-reconstituted MRP4, the molecular structures of the transporter in complex with substrates (obtained from samples in which “active turnover conditions”^{51,52} are mimicked, see [STAR Methods](#) for details) are *globally* indistinguishable from the molecular structures obtained from samples of nanodisc-reconstituted MRP4 to which no substrate has been added ([Figures S12, S2, and S4–S6](#)). This contrasts with what is observed from cryo-EM studies of bovine MRP1,⁴⁶ where presence of the native substrate, leukotriene C4 (LTC4), appears to induce a distinct relative conformational shift, effectively decreasing the inter-NBD distance ([Figure S12](#)).

From recent structural studies,^{25,46,53} evidence is accumulating that ligand binding at the substrate-binding pockets of ABC exporters affects conformational cycling mainly by altering the relative positioning of the NBDs. Substrate binding may positively modulate ATPase activity by promoting NBD dimerization,^{25,46} which would explain the observation that the ATPase activity of most ABC exporters is stimulated by the presence of substrate.⁵⁴ However, not all substrates of all exporters stimulate ATP hydrolysis,⁴¹ and major relative NBD repositioning is not observed in all substrate-bound structures.⁵⁵

The inward to outward-facing transition

According to the alternating access model,⁵⁶ ABC transporters move substrates across cellular membranes by switching between IF and OF states, alternately exposing a central binding pocket to opposite sides of the membrane.^{57,58} Canonically, the “resting” state of type IV exporters is the IF conformation,² in which the binding pocket is open toward the cytoplasm. Following ATP binding, NBD dimerization causes the exporter to transition into an OF configuration, in which the binding pocket is inaccessible from inside the cell but can be open toward the extracellular side. After ATP hydrolysis, the NBDs dissociate and the exporter returns to its resting state.

Like other ABC transporters, nanodisc-reconstituted hMRP4 and detergent-reconstituted bMRP1 display significant basal ATPase activity,⁴⁶ indicating that both reconstituted transporters can undergo conformational cycling even in the absence of substrate. It is nonetheless interesting to observe that nanodisc-reconstituted EQ hMRP4 was found to favor an OF *occluded* conformation, while the equivalent mutant variant of detergent-reconstituted bMRP1 (E1454Q bMRP1) favored an OF *open* conformation⁴⁴ ([Figure S12](#)). Even wild-type (detergent-reconstituted) bMRP1 under active turnover conditions⁵¹ favored the same *open* OF conformation, while wild-type (nanodisc-reconstituted) hMRP4 under similar active turnover conditions is found exclusively in an IF conformation. Given the widely different reconstitution conditions used for the respective studies of the two different proteins, it is not entirely surprising that they exhibit different conformational landscapes. However, to what extent this difference in conformational preference reflects the effects of the different reconstitution environments remains to be elucidated.

The MRP open-occluded isomerization

Neither of the resolved OF structures of hMRP4 and bMRP1 feature bound substrates, despite the same substrates as those of the samples used to obtain the respective substrate-bound structures being present at practically the same concentrations. In the OF occluded conformation of hMRP4, the substrate-binding pocket is sealed off and fully collapsed ([Figure S13A](#)), while in the OF open conformation of bMRP1, the pocket is partly accessible from the extracellular side but rearranged relative to the IF conformations.⁴⁴ While both transporters exhibit lateral displacement of their transmembrane helices upon IF-OF transitioning ([Figure S13B](#)), the helix positioning of the occluded conformation most closely resembles an IF configuration. It is therefore likely that the OF occluded conformation of hMRP4 represents a structural state on the MRP transport cycle trajectory closer to transporter resetting (OF-IF transitioning) than the OF open conformation of bMRP1. Interestingly, judging by the relative lateral IF-OF shifts of the hMRP4 and bMRP1 transmembrane helices, open-occluded isomerization appears to involve an asymmetric 8/4 movement of equivalent helices ([Figure S13C](#)) rather than a pseudo-symmetric 6/6 movement of the two transmembrane bundles.

The structure of OF occluded hMRP4 is overall highly similar to the resolved OF occluded structures of other ABC transporters: The NBD arrangement and distance between key residues of the nucleotide-binding sites are practically identical for the compared structures ([Figure S14A](#)), regardless of number of consensus sites or whether the transporters are monomers or dimers. The structural differences between the OF occluded structures become more apparent upon isolated comparison of the TMD segments ([Figure S14B](#)): While F352 and S984 of hMRP4 (highly conserved among the MRPs) from opposing transmembrane helices 6 and 12 appear to form an extracellular gate in hMRP4, equivalent residues do not appear to serve the same function in the compared transporters. However, equivalent helices of the asymmetric heterodimer TmrAB serve a “gate-keeper” function,⁵² while the “gate region” of OF occluded ABCB1 (and by extension ABCB4)^{25,27} is highly similar to the equivalent region of hMRP4, reflected in quantitatively high similarity ([Figures S14A and S14B](#)).

MRP substrate discrimination

The substrate-binding pockets of hMRP4 and bMRP1 share a similar bipartite architecture ([Figures S15A and S15B](#)), which is reflected in similarities in the substrate profiles of the two homologous transporters: Both exporters preferentially transport organic anions, including metabolic conjugates of GSH, glucuronide, and sulfate (e.g., LTC4, E17βG, and DHEAS, respectively),^{59–62} and along with other MRPs, both MRP4 and MRP1 also transport MTX.^{15,63}

MTX transport by MRP4 has previously been shown to be effectively eliminated by alanine substitutions of W995 and R998,^{64,65} which is confirmed in this study, where also the R946A and Q994A mutations are shown to significantly reduce MTX efflux by MRP4. Mutation of W1246 and N1245 of hMRP1 (equivalent to W995 and Q994 of hMRP4 and W1245 and N1244 of bMRP1) selectively eliminates E17βG transport without affecting LTC4 transport,^{66,67} and charge reversal of R1197 and R1249 of hMRP1 (equivalent to R946 and R998 of hMRP4 and

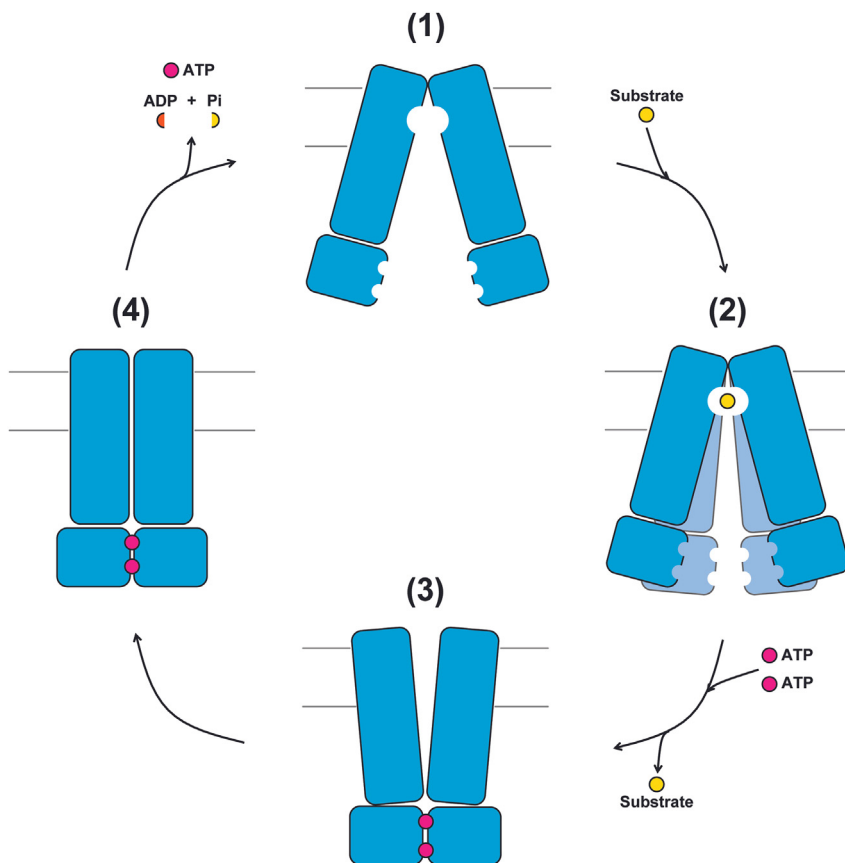


Figure 5. The MRP transport cycle

Cartoon representation of general features of the MRP transport cycle. At least four distinct states have so far been structurally resolved for the MRPs: (1) an IF resting state (for hMRP4 (this study) and bMRP1⁴⁶); (2) an IF substrate-bound state (for hMRP4 (this study) and bMRP1⁴⁶); (3) an OF open (post-substrate release) state (for bMRP1⁴⁴), and (4) an OF occluded state (for hMRP4 (this study)). While substrate is not necessary for IF-OF transitioning (and its binding does not necessarily effect drastic structural changes), the presence of ATP is apparently required to reach (3), which appears to isomerize with (4). For the asymmetric MRPs (with one nucleotide binding site being degenerate), the (4)-(1) transition (transporter resetting) involves hydrolysis of at least one ATP molecule and release of the produced ADP and orthophosphate (P_i).

Both MRP4 and MRP1 transport GSH conjugates, which are reflected in the similar spatial arrangement of equivalent P-pocket residues that in bMRP1 coordinate the GSH moiety of LTC₄. PGE₂ appears to be capable of being coordinated by the hMRP4 P-pocket residues similar to how LTC₄ is coordinated by bMRP1 (Figure S15B), with the two substrates engaging in equivalent interactions with equivalent residues from both transmembrane bundles. However, while LTC₄ is a

high-affinity substrate of both transporters,^{62,69} PGE₂ is transported with a much higher efficiency by MRP4 compared to other MRPs and does not appear to be a substrate of MRP1.⁷⁰ Interestingly, the residues of the hydrophobic sandwich of MRP4 surround the uncharged moiety of PGE₂ and may provide the necessary coordination conditions absent in MRP1.

While both MTX and PGE₂ appear to interact with residues of both transmembrane bundles of MRP4, their coordination is different (Figure 3), which may explain why PGE₂ strongly stimulates basal ATPase activity, and MTX only moderately stimulates activity. The demonstration in this study that TPT *decreases* ATPase activity of MRP4 to below basal levels, which is also observed for nanodisc-reconstituted ABCG2,⁴¹ may be explained by the observation that TPT does not appear to be as extensively coordinated as the other substrates, and seemingly associates closely with only two residues of the substrate-binding pocket that nonetheless belong to separate transmembrane bundles.

R1196 and R1248 of bMRP1) effectively eliminates not only LTC₄ transport but also transport of E17βG and MTX.⁶⁸ Even like-charge substitutions of these residues result in very low MTX transport, and the R998K hMRP4 variant is likewise practically unable to transport MTX,⁶⁴ hinting at a general role of these residue positions in MRP substrate discrimination.

F368 sits at the center of the binding pocket (Figure 3), and the F368A mutation has previously been shown to effectively eliminate transport of MTX.⁶⁴ The neighboring L367 constitutes a unique polypeptide extension among the MRPs (Figure S15C) and is the only binding-pocket residue apart from W995 appearing to be directly involved in coordination of TPT (Figure 3). These two residues (along with F368) appear to form a hydrophobic sandwich similar to the substrate-coordinating phenyl group sandwich of ABCG2,^{36–39} which interestingly enough also binds TPT.⁴¹ As shown in this study, individual alanine-substitution of all three of these “sandwich residues” negatively affects MTX efflux, indicating that the exact residue identities of these positions are crucial for proper binding of MTX and potentially TPT and other substrates.

The H152A and K106A hMRP4 variants exhibit clear resistance phenotypes (Figure S11) despite apparently being expressed at relatively lower levels as judged by Western blotting (Figure 4D). This observation at least indicates that the MTX translocation of hMRP4 is not negatively modulated by introduction of these mutations and that the exact identities of the corresponding residues are not strictly necessary for achieving normal levels of MTX efflux efficiency.

The MRP transport cycle

Comparing the obtained structures of MRP4 and MRP1 in light of the accumulated biochemical evidence from functional and mutational analyses of both transporters, we greatly expand our general understanding of the structural and mechanistic basis of the general MRP transport cycle.

While both MRPs display significant basal ATPase activity differentially modulated by the presence of substrates, lipid molecules also appear to affect conformational cycling, reflected in

the sensitivity to different reconstitution conditions, and the observation that structures of both transporters feature annular lipids.

The two MRPs exhibit a remarkably similar binding pocket architecture in which the relatively conserved, positively charged P-pocket section may account for substantial substrate profile overlap, while structural differences in other parts of the binding pocket mainly account for substrate profile variation among the MRPs. In MRP4, a tight, hydrophobic sandwich, located at the interface of the two pocket sections, appears to be a strong determinant of MRP4 substrate specificity involved in coordination of both TPT and PGE2, neither of which appear to be substrates of MRP1.^{70,71}

The OF occluded conformation of nanodisc-reconstituted hMRP4 presented in this study has, to our knowledge, never before been resolved for any MRP and likely corresponds to a structural state that must be assumed before transporter resetting can occur^{2,52} (Figure 5). OF open-occluded isomerization of MRPs practically constitutes opening and closing of a conserved extracellular gate and appears to involve an asymmetric lateral rearrangement of transmembrane helices.

Many details of the conformational trajectory of the MRP transport cycle remain unclear, including the exact mechanism of the allosteric coupling between the binding pocket and the NBDs, and how specifically the interactions between the TMDs and lipid molecules affect conformational cycling. We expect future functional and structural studies to bring us even closer to a general understanding of the physiologically and therapeutically important MRPs.

STAR★METHODS

Detailed methods are provided in the online version of this paper and include the following:

- [KEY RESOURCES TABLE](#)
- [RESOURCE AVAILABILITY](#)
 - Lead contact
 - Materials availability
 - Data and code availability
- [EXPERIMENTAL MODEL AND STUDY PARTICIPANT DETAILS](#)
 - Cell lines
- [METHOD DETAILS](#)
 - Protein expression and purification
 - Nanodisc reconstitution
 - ATPase activity assays
 - Drug susceptibility assay
 - Electron microscopy sample preparation
 - Cryo-EM data collection and processing
- [MODEL BUILDING AND REFINEMENT](#)
 - Figure preparation
- [QUANTIFICATION AND STATISTICAL ANALYSIS](#)

SUPPLEMENTAL INFORMATION

Supplemental information can be found online at <https://doi.org/10.1016/j.str.2023.08.014>.

ACKNOWLEDGMENTS

The Novo Nordisk Foundation Center for Protein Research is supported financially by the Novo Nordisk Foundation (grant NNF14CC0001). This work was also supported by an NNF Hallas-Møller Emerging Investigator (NNF17OC0031006). N.M.I.T. is a member of the Integrative Structural Biology Cluster (ISBUC) at the University of Copenhagen. M.B. acknowledges the Neye Foundation for support. We thank the Danish Cryo-EM Facility at the Core Facility for Integrated Microscopy (CFIM) at the University of Copenhagen. Part of the data processing was performed at the Computerome, the Danish National Computer for Life Sciences.

We thank Katharina Duerr (University of Oxford) for kindly supplying us with a vial of the purified pHTBV1.1 vector, Jonathan Elegheert (IINS) for kindly supplying us with the expression plasmid for the HRV3C protease (as well as protocols for expression and purification), and Kenneth A. Matreyek (Case Western Reserve University) for kindly supplying vials of the parental HEK293T LLP-Int-Blast cell line, as well as protocols for maintaining and establishing derivative cell lines.

AUTHOR CONTRIBUTIONS

M.B. and N.M.I.T. conceptualized the research project and planned the experiments.

M.B. carried out all expressions, purifications, and sample preparations for electron microscopy and ATPase activity assays and analyzed the data.

T.P. and M.B. collected and analyzed the electron microscopy data.

I.R. and M.B. built, refined, and validated the structural models.

M.B. conducted the cellular drug susceptibility assays and analyzed the data.

I.R. and M.B. carried out all molecular cloning and generated the derivative stable cell lines.

M.B. wrote the first draft of the paper and prepared all the figures together with N.M.I.T.

All authors contributed to the revision of the manuscript.

DECLARATION OF INTERESTS

The authors declare no competing interests.

INCLUSION AND DIVERSITY

We support inclusive, diverse, and equitable conduct of research.

Received: December 8, 2022

Revised: May 31, 2023

Accepted: August 14, 2023

Published: September 7, 2023

REFERENCES

1. Dean, M., Rzhetsky, A., and Allikmets, R. (2001). The human ATP-binding cassette (ABC) transporter superfamily. *Genome Res.* 11, 1156–1166. <https://doi.org/10.1101/gr.184901>.
2. Thomas, C., and Tampé, R. (2020). Structural and Mechanistic Principles of ABC Transporters. *Annu. Rev. Biochem.* 89, 605–636. <https://doi.org/10.1146/ANNUREV-BIOCHEM-011520-105201>.
3. Ween, M.P., Armstrong, M.A., Oehler, M.K., and Ricciardelli, C. (2015). The role of ABC transporters in ovarian cancer progression and chemoresistance. *Crit. Rev. Oncol. Hematol.* 96, 220–256. <https://doi.org/10.1016/J.CRITREVONC.2015.05.012>.
4. Nies, A.T., Jedlitschky, G., König, J., Herold-Mende, C., Steiner, H.H., Schmitt, H.P., and Keppler, D. (2004). Expression and immunolocalization of the multidrug resistance proteins, MRP1-MRP6 (ABCC1-ABCC6), in human brain. *Neuroscience* 129, 349–360. <https://doi.org/10.1016/J.NEUROSCIENCE.2004.07.051>.
5. Leggas, M., Adachi, M., Scheffer, G.L., Sun, D., Wielinga, P., Du, G., Mercer, K.E., Zhuang, Y., Panetta, J.C., Johnston, B., et al. (2004). MRP4 confers resistance to topotecan and protects the brain from

- chemotherapy. *Mol. Cell Biol.* 24, 7612–7621. <https://doi.org/10.1128/MCB.24.17.7612-7621.2004>.
6. Russel, F.G.M., Koenderink, J.B., and Masereeuw, R. (2008). Multidrug resistance protein 4 (MRP4/ABCC4): a versatile efflux transporter for drugs and signalling molecules. *Trends Pharmacol. Sci.* 29, 200–207. <https://doi.org/10.1016/J.TIPS.2008.01.006>.
 7. Sodani, K., Patel, A., Kathawala, R.J., and Chen, Z.S. (2012). Multidrug resistance associated proteins in multidrug resistance. *Chin. J. Cancer* 37, 58–72. <https://doi.org/10.5732/CJC.011.10329>.
 8. Norris, M.D., Smith, J., Tanabe, K., Tobin, P., Flemming, C., Scheffer, G.L., Wielinga, P., Cohn, S.L., London, W.B., Marshall, G.M., et al. (2005). Expression of multidrug transporter MRP4/ABCC4 is a marker of poor prognosis in neuroblastoma and confers resistance to irinotecan in vitro. *Mol. Cancer Therapeut.* 4, 547–553. <https://doi.org/10.1158/1535-7163.MCT-04-0161>.
 9. Borel, F., Han, R., Visser, A., Petry, H., van Deventer, S.J.H., Jansen, P.L.M., and Konstantinova, P.; Réseau Centre de Ressources Biologiques Foie French Liver Biobanks Network, France (2012). Adenosine triphosphate-binding cassette transporter genes up-regulation in untreated hepatocellular carcinoma is mediated by cellular microRNAs. *Hepatology* 55, 821–832. <https://doi.org/10.1002/HEP.24682>.
 10. Zhao, X., Guo, Y., Yue, W., Zhang, L., Gu, M., and Wang, Y. (2014). ABCC4 is required for cell proliferation and tumorigenesis in non-small cell lung cancer. *OncoTargets Ther.* 7, 343–351. <https://doi.org/10.2147/OTT.S56029>.
 11. Hlaváč, V., Brynychová, V., Václavíková, R., Ehrlichová, M., Vrána, D., Pecha, V., Koževnikovová, R., Trnková, M., Gaték, J., Kopperová, D., et al. (2013). The expression profile of ATP-binding cassette transporter genes in breast carcinoma. *Pharmacogenomics* 14, 515–529. <https://doi.org/10.2217/PGS.13.26>.
 12. Ho, L.L., Kench, J.G., Handelsman, D.J., Scheffer, G.L., Stricker, P.D., Grygiel, J.G., Sutherland, R.L., Henshall, S.M., Allen, J.D., and Horvath, L.G. (2008). Androgen regulation of multidrug resistance-associated protein 4 (MRP4/ABCC4) in prostate cancer. *Prostate* 68, 1421–1429. <https://doi.org/10.1002/PROS.20809>.
 13. Chen, Z.S., Lee, K., and Kruh, G.D. (2001). Transport of cyclic nucleotides and estradiol 17-beta-D-glucuronide by multidrug resistance protein 4. Resistance to 6-mercaptopurine and 6-thioguanine. *J. Biol. Chem.* 276, 33747–33754. <https://doi.org/10.1074/JBC.M104833200>.
 14. Ruel, N.M., Nguyen, K.H., Vilas, G., and Hammond, J.R. (2019). Characterization of 6-Mercaptopurine Transport by the SLC43A3-Encoded Nucleobase Transporter. *Mol. Pharmacol.* 95, 584–596. <https://doi.org/10.1124/MOL.118.114389>.
 15. Lee, K., Klein-Szanto, A.J., and Kruh, G.D. (2000). Analysis of the MRP4 drug resistance profile in transfected NIH3T3 cells. *J. Natl. Cancer Inst.* 92, 1934–1940. <https://doi.org/10.1093/JNCI/92.23.1934>.
 16. Tian, Q., Zhang, J., Chan, S.Y., Tan, T.M.C., Duan, W., Huang, M., Zhu, Y.Z., Chan, E., Yu, Q., Nie, Y.Q., et al. (2006). Topotecan is a substrate for multidrug resistance associated protein 4. *Curr. Drug Metabol.* 7, 105–118. <https://doi.org/10.2174/138920006774832550>.
 17. Schuetz, J.D., Connelly, M.C., Sun, D., Paibir, S.G., Flynn, P.M., Srinivas, R.v., Kumar, A., and Fridland, A. (1999). MRP4: A previously unidentified factor in resistance to nucleoside-based antiviral drugs. *Nat. Med.* 5, 1048–1051. <https://doi.org/10.1038/12487>.
 18. Adachi, M., Sampath, J., Lan, L.b., Sun, D., Hargrove, P., Flatley, R., Tatum, A., Edwards, M.Z., Wezeman, M., Matherly, L., et al. (2002). Expression of MRP4 confers resistance to ganciclovir and compromises bystander cell killing. *J. Biol. Chem.* 277, 38998–39004. <https://doi.org/10.1074/JBC.M203262200>.
 19. Imaoka, T., Kusuhara, H., Adachi, M., Schuetz, J.D., Takeuchi, K., and Sugiyama, Y. (2007). Functional involvement of multidrug resistance-associated protein 4 (MRP4/ABCC4) in the renal elimination of the antiviral drugs adefovir and tenofovir. *Mol. Pharmacol.* 71, 619–627. <https://doi.org/10.1124/MOL.106.028233>.
 20. Ci, L., Kusuhara, H., Adachi, M., Schuetz, J.D., Takeuchi, K., and Sugiyama, Y. (2007). Involvement of MRP4 (ABCC4) in the luminal efflux of ceftizoxime and cefazolin in the kidney. *Mol. Pharmacol.* 71, 1591–1597. <https://doi.org/10.1124/MOL.106.031823>.
 21. Akanuma, S.I., Uchida, Y., Ohtsuki, S., Kamiie, J.I., Tachikawa, M., Terasaki, T., and Hosoya, K.I. (2011). Molecular-weight-dependent, anionic-substrate-preferential transport of β -lactam antibiotics via multidrug resistance-associated protein 4. *Drug Metabol. Pharmacokin.* 26, 602–611. <https://doi.org/10.2133/DMPK.DMPK-11-RG-063>.
 22. Zamek-Gliszczynski, M.J., Taub, M.E., Chothe, P.P., Chu, X., Giacomini, K.M., Kim, R.B., Ray, A.S., Stocker, S.L., Unadkat, J.D., Wittwer, M.B., et al. (2018). Transporters in Drug Development: 2018 ITC Recommendations for Transporters of Emerging Clinical Importance. *Clin. Pharmacol. Ther.* 104, 890–899. <https://doi.org/10.1002/CPT.1112>.
 23. In Vitro Drug Interaction Studies: Cytochrome P-450 Enzyme- and Transporter-Mediated Drug Interactions - Digital Collections - National Library of Medicine. <https://collections.nlm.nih.gov/catalog.nlm.nlmuid-101767646-pdf>.
 24. Kim, Y., and Chen, J. (2018). Molecular structure of human P-glycoprotein in the ATP-bound, outward-facing conformation. *Science* 359, 915–919. <https://doi.org/10.1126/SCIENCE.AAR7389>.
 25. Alam, A., Kowal, J., Broude, E., Roninson, I., and Locher, K.P. (2019). Structural insight into substrate and inhibitor discrimination by human P-glycoprotein. *Science* 363, 753–756. <https://doi.org/10.1126/SCIENCE.AAV7102>.
 26. Oldham, M.L., Grigorieff, N., and Chen, J. (2016). Structure of the transporter associated with antigen processing trapped by herpes simplex virus. *Elife* 5, e21829. <https://doi.org/10.7554/ELIFE.21829>.
 27. Olsen, J.A., Alam, A., Kowal, J., Stieger, B., and Locher, K.P. (2020). Structure of the human lipid exporter ABCB4 in a lipid environment. *Nat. Struct. Mol. Biol.* 27, 62–70. <https://doi.org/10.1038/S41594-019-0354-3>.
 28. Nosol, K., Bang-Sørensen, R., Irobalieva, R.N., Erramilli, S.K., Stieger, B., Kossiakoff, A.A., and Locher, K.P. (2021). Structures of ABCB4 provide insight into phosphatidylcholine translocation. *Proc. Natl. Acad. Sci. USA* 118, e2106702118. <https://doi.org/10.1073/PNAS.2106702118>.
 29. Wang, C., Cao, C., Wang, N., Wang, X., Wang, X., and Zhang, X.C. (2020). Cryo-electron microscopy structure of human ABCB6 transporter. *Protein Sci.* 29, 2363–2374. <https://doi.org/10.1002/PRO.3960>.
 30. Kim, S., Lee, S.S., Park, J.G., Kim, J.W., Ju, S., Choi, S.H., Kim, S., Kim, N.J., Hong, S., Kang, J.Y., and Jin, M.S. (2022). Structural Insights into Porphyrin Recognition by the Human ATP-Binding Cassette Transporter ABCB6. *Mol. Cell.* 45, 575–587. <https://doi.org/10.14348/MOLCELLS.2022.0040>.
 31. Yan, Q., Shen, Y., and Yang, X. (2022). Cryo-EM structure of AMP-PNP-bound human mitochondrial ATP-binding cassette transporter ABCB7. *J. Struct. Biol.* 214, 107832. <https://doi.org/10.1016/J.JSB.2022.107832>.
 32. Li, S., Ren, Y., Lu, X., Shen, Y., and Yang, X. (2021). Cryo-EM structure of human ABCB8 transporter in nucleotide binding state. *Biochem. Biophys. Res. Commun.* 557, 187–191. <https://doi.org/10.1016/J.BBRC.2021.04.007>.
 33. Wang, L., Hou, W.T., Chen, L., Jiang, Y.L., Xu, D., Sun, L., Zhou, C.Z., and Chen, Y. (2020). Cryo-EM structure of human bile salts exporter ABCB11. *Cell Res.* 30, 623–625. <https://doi.org/10.1038/S41422-020-0302-0>.
 34. Wang, L., Hou, W.T., Wang, J., Xu, D., Guo, C., Sun, L., Ruan, K., Zhou, C.Z., and Chen, Y. (2022). Structures of human bile acid exporter ABCB11 reveal a transport mechanism facilitated by two tandem substrate-binding pockets. *Cell Res.* 32, 501–504. <https://doi.org/10.1038/S41422-021-00611-9>.
 35. Sun, Y., Wang, J., Long, T., Qi, X., Donnelly, L., Elghobashi-Meinhardt, N., Esparza, L., Cohen, J.C., Xie, X.S., Hobbs, H.H., and Li, X. (2021). Molecular basis of cholesterol efflux via ABCG subfamily transporters. *Proc. Natl. Acad. Sci. USA* 118, e2110483118. <https://doi.org/10.1073/PNAS.2110483118>.

36. Taylor, N.M.I., Manolaridis, I., Jackson, S.M., Kowal, J., Stahlberg, H., and Locher, K.P. (2017). Structure of the human multidrug transporter ABCG2. *Nature* 546, 504–509. <https://doi.org/10.1038/NATURE22345>.
37. Jackson, S.M., Manolaridis, I., Kowal, J., Zechner, M., Taylor, N.M.I., Bause, M., Bauer, S., Bartholomaeus, R., Bernhardt, G., Koenig, B., et al. (2018). Structural basis of small-molecule inhibition of human multidrug transporter ABCG2. *Nat. Struct. Mol. Biol.* 25, 333–340. <https://doi.org/10.1038/S41594-018-0049-1>.
38. Manolaridis, I., Jackson, S.M., Taylor, N.M.I., Kowal, J., Stahlberg, H., and Locher, K.P. (2018). Cryo-EM structures of a human ABCG2 mutant trapped in ATP-bound and substrate-bound states. *Nature* 563, 426–430. <https://doi.org/10.1038/S41586-018-0680-3>.
39. Orlando, B.J., and Liao, M. (2020). ABCG2 transports anticancer drugs via a closed-to-open switch. *Nat. Commun.* 11, 2264. <https://doi.org/10.1038/S41467-020-16155-2>.
40. Kowal, J., Ni, D., Jackson, S.M., Manolaridis, I., Stahlberg, H., and Locher, K.P. (2021). Structural Basis of Drug Recognition by the Multidrug Transporter ABCG2. *J. Mol. Biol.* 433, 166980. <https://doi.org/10.1016/J.JMB.2021.166980>.
41. Yu, Q., Ni, D., Kowal, J., Manolaridis, I., Jackson, S.M., Stahlberg, H., and Locher, K.P. (2021). Structures of ABCG2 under turnover conditions reveal a key step in the drug transport mechanism. *Nat. Commun.* 12, 4376. <https://doi.org/10.1038/S41467-021-24651-2>.
42. Hegedüs, T., Sessler, T., Scott, R., Thelin, W., Bakos, É., Váradi, A., Szabó, K., Homolya, L., Milgram, S.L., and Sarkadi, B. (2003). C-terminal phosphorylation of MRP2 modulates its interaction with PDZ proteins. *Biochem. Biophys. Res. Commun.* 302, 454–461. [https://doi.org/10.1016/S0006-291X\(03\)00196-7](https://doi.org/10.1016/S0006-291X(03)00196-7).
43. Moody, J.E., Millen, L., Binns, D., Hunt, J.F., and Thomas, P.J. (2002). Cooperative, ATP-dependent association of the nucleotide binding cassettes during the catalytic cycle of ATP-binding cassette transporters. *J. Biol. Chem.* 277, 21111–21114. <https://doi.org/10.1074/JBC.C200228200>.
44. Johnson, Z.L., and Chen, J. (2018). ATP Binding Enables Substrate Release from Multidrug Resistance Protein 1. *Cell* 172, 81–89. <https://doi.org/10.1016/J.CELL.2017.12.005>.
45. Henriksen, U., Gether, U., and Litman, T. (2005). Effect of Walker A mutation (K86M) on oligomerization and surface targeting of the multidrug resistance transporter ABCG2. *J. Cell Sci.* 118, 1417–1426. <https://doi.org/10.1242/JCS.01729>.
46. Johnson, Z.L., and Chen, J. (2017). Structural Basis of Substrate Recognition by the Multidrug Resistance Protein MRP1. *Cell* 168, 1075–1085. <https://doi.org/10.1016/J.CELL.2017.01.041>.
47. Mi, W., Li, Y., Yoon, S.H., Ernst, R.K., Walz, T., and Liao, M. (2017). Structural basis of MsbA-mediated lipopolysaccharide transport. *Nature* 549, 233–237. <https://doi.org/10.1038/NATURE23649>.
48. Thélot, F.A., Zhang, W., Song, K., Xu, C., Huang, J., and Liao, M. (2021). Distinct allosteric mechanisms of first-generation MsbA inhibitors. *Science* 374, 580–585. <https://doi.org/10.1126/SCIENCE.ABI9009>.
49. Alvarez, F.J.D., Orelle, C., Huang, Y., Bajaj, R., Everly, R.M., Klug, C.S., and Davidson, A.L. (2015). Full engagement of liganded maltose-binding protein stabilizes a semi-open ATP-binding cassette dimer in the maltose transporter. *Mol. Microbiol.* 98, 878–894. <https://doi.org/10.1111/MMI.13165>.
50. Shukla, S., Abel, B., Chufan, E.E., and Ambudkar, S.v. (2017). Effects of a detergent micelle environment on P-glycoprotein (ABCB1)-ligand interactions. *J. Biol. Chem.* 292, 7066–7076. <https://doi.org/10.1074/JBC.M116.771634>.
51. Wang, L., Johnson, Z.L., Wasserman, M.R., Levring, J., Chen, J., and Liu, S. (2020). Characterization of the kinetic cycle of an ABC transporter by single-molecule and cryo-EM analyses. *Elife* 9, e56451. <https://doi.org/10.7554/ELIFE.56451>.
52. Hofmann, S., Janulienė, D., Mehdipour, A.R., Thomas, C., Stefan, E., Brüchert, S., Kuhn, B.T., Geertsma, E.R., Hummer, G., Tampé, R., and Moeller, A. (2019). Conformation space of a heterodimeric ABC exporter under turnover conditions. *Nature* 571, 580–583. <https://doi.org/10.1038/S41586-019-1391-0>.
53. Ho, H., Miu, A., Alexander, M.K., Garcia, N.K., Oh, A., Zilberleyb, I., Reichelt, M., Austin, C.D., Tam, C., Shriver, S., et al. (2018). Structural basis for dual-mode inhibition of the ABC transporter MsbA. *Nature* 557, 196–201. <https://doi.org/10.1038/S41586-018-0083-5>.
54. Lewinson, O., Orelle, C., and Seeger, M.A. (2020). Structures of ABC transporters: handle with care. *FEBS Lett.* 594, 3799–3814. <https://doi.org/10.1002/1873-3468.13966>.
55. Lee, J.Y., Yang, J.G., Zhitnitsky, D., Lewinson, O., and Rees, D.C. (2014). Structural basis for heavy metal detoxification by an Atm1-type ABC exporter. *Science* 343, 1133–1136. <https://doi.org/10.1126/SCIENCE.1246489>.
56. Jardetzky, O. (1966). Simple allosteric model for membrane pumps. *Nature* 211, 969–970. <https://doi.org/10.1038/211969A0>.
57. Callaghan, R., Ford, R.C., and Kerr, I.D. (2006). The translocation mechanism of P-glycoprotein. *FEBS Lett.* 580, 1056–1063. <https://doi.org/10.1016/J.FEBSLET.2005.11.083>.
58. Szöllösi, D., Rose-Sperling, D., Hellmich, U.A., and Stockner, T. (2018). Comparison of mechanistic transport cycle models of ABC exporters. *Biochim. Biophys. Acta Biomembr.* 1860, 818–832. <https://doi.org/10.1016/J.BBAMEM.2017.10.028>.
59. Jedlitschky, G., Leier, I., Buchholz, U., Center, M., and Keppler, D. (1994). ATP-dependent transport of glutathione S-conjugates by the multidrug resistance-associated protein. *Cancer Res.* 54, 4833–4836.
60. Jedlitschky, G., Leier, I., Buchholz, U., Barnouin, K., Kurz, G., and Keppler, D. (1996). Transport of glutathione, glucuronate, and sulfate conjugates by the MRP gene-encoded conjugate export pump. *Cancer Res.* 56, 988–994.
61. Zelcer, N., Reid, G., Wielinga, P., Kuil, A., van der Heijden, I., Schuetz, J.D., and Borst, P. (2003). Steroid and bile acid conjugates are substrates of human multidrug-resistance protein (MRP) 4 (ATP-binding cassette C4). *Biochem. J.* 371, 361–367. <https://doi.org/10.1042/BJ20021886>.
62. Rius, M., Hummel-Eisenbeiss, J., and Keppler, D. (2008). ATP-dependent transport of leukotrienes B4 and C4 by the multidrug resistance protein ABCC4 (MRP4). *J. Pharmacol. Exp. Therapeut.* 324, 86–94. <https://doi.org/10.1124/JPET.107.131342>.
63. Hooijberg, J.H., Broxterman, H.J., Kool, M., Assaraf, Y.G., Peters, G.J., Noordhuis, P., Scheper, R.J., Borst, P., Pinedo, H.M., and Jansen, G. (1999). Antifolate resistance mediated by the multidrug resistance proteins MRP1 and MRP2. *Cancer Res.* 59, 2532–2535.
64. Wittgen, H.G.M., van den Heuvel, J.J.M.W., Krieger, E., Schaftenaar, G., Russel, F.G.M., and Koenderink, J.B. (2012). Phenylalanine 368 of multidrug resistance-associated protein 4 (MRP4/ABCC4) plays a crucial role in substrate-specific transport activity. *Biochem. Pharmacol.* 84, 366–373. <https://doi.org/10.1016/J.BCP.2012.04.012>.
65. El-Sheikh, A.A.K., van den Heuvel, J.J.M.W., Krieger, E., Russel, F.G.M., and Koenderink, J.B. (2008). Functional role of arginine 375 in transmembrane helix 6 of multidrug resistance protein 4 (MRP4/ABCC4). *Mol. Pharmacol.* 74, 964–971. <https://doi.org/10.1124/MOL.107.043661>.
66. Ito, K., Olsen, S.L., Qiu, W., Deeley, R.G., and Cole, S.P. (2001). Mutation of a single conserved tryptophan in multidrug resistance protein 1 (MRP1/ABCC1) results in loss of drug resistance and selective loss of organic anion transport. *J. Biol. Chem.* 276, 15616–15624. <https://doi.org/10.1074/JBC.M011246200>.
67. Zhang, D.-W., Cole, S.P.C., and Deeley, R.G. (2002). Determinants of the Substrate Specificity of Multidrug Resistance Protein 1. *J. Biol. Chem.* 277, 20934–20941. <https://doi.org/10.1074/jbc.m201311200>.
68. Situ, D., Haimeur, A., Conseil, G., Sparks, K.E., Zhang, D., Deeley, R.G., and Cole, S.P.C. (2004). Mutational analysis of ionizable residues proximal to the cytoplasmic interface of membrane spanning domain 3 of the multidrug resistance protein, MRP1 (ABCC1): glutamate 1204 is important for both the expression and catalytic activity of the transporter. *J. Biol. Chem.* 279, 38871–38880. <https://doi.org/10.1074/JBC.M403832200>.

69. Loe, D.W., Almquist, K.C., Deeley, R.G., and Cole, S.P. (1996). Multidrug resistance protein (MRP)-mediated transport of leukotriene C4 and chemotherapeutic agents in membrane vesicles. Demonstration of glutathione-dependent vincristine transport. *J. Biol. Chem.* *271*, 9675–9682. <https://doi.org/10.1074/JBC.271.16.9675>.
70. Reid, G., Wielinga, P., Zelcer, N., van der Heijden, I., Kuil, A., de Haas, M., Wijnholds, J., and Borst, P. (2003). The human multidrug resistance protein MRP4 functions as a prostaglandin efflux transporter and is inhibited by nonsteroidal antiinflammatory drugs. *Proc. Natl. Acad. Sci. USA* *100*, 9244–9249. <https://doi.org/10.1073/PNAS.1033060100>.
71. Horowitz, N.S., Hua, J., Gibb, R.K., Mutch, D.G., and Herzog, T.J. (2004). The role of topotecan for extending the platinum-free interval in recurrent ovarian cancer: An in vitro model. *Gynecol. Oncol.* *94*, 67–73. <https://doi.org/10.1016/j.ygyno.2004.03.047>.
72. Kyte, J., and Doolittle, R.F. (1982). A simple method for displaying the hydropathic character of a protein. *J. Mol. Biol.* *157*, 105–132. [https://doi.org/10.1016/0022-2836\(82\)90515-0](https://doi.org/10.1016/0022-2836(82)90515-0).
73. Fornwald, J.A., Lu, Q., Boyce, F.M., and Ames, R.S. (2016). Gene Expression in Mammalian Cells Using BacMam, a Modified Baculovirus System. *Methods Mol. Biol.* *1350*, 95–116. https://doi.org/10.1007/978-1-4939-3043-2_5.
74. Steck, T.L., and Lange, Y. (2018). Transverse distribution of plasma membrane bilayer cholesterol: Picking sides. *Traffic* *19*, 750–760. <https://doi.org/10.1111/TRA.12586>.
75. Bayburt, T.H., Grinkova, Y.v., and Sligar, S.G. (2002). Self-Assembly of Discoidal Phospholipid Bilayer Nanoparticles with Membrane Scaffold Proteins. *Nano Lett.* *2*, 853–856. https://doi.org/10.1021/NL025623K/SUPPL_FILE/NL025623K_S1.PDF.
76. Matreyek, K.A., Stephany, J.J., Chiasson, M.A., Hasle, N., and Fowler, D.M. (2020). An improved platform for functional assessment of large protein libraries in mammalian cells. *Nucleic Acids Res.* *48*, e1. <https://doi.org/10.1093/NAR/GKZ910>.
77. Punjani, A., Rubinstein, J.L., Fleet, D.J., and Brubaker, M.A. (2017). cryoSPARC: algorithms for rapid unsupervised cryo-EM structure determination. *Nat. Methods* *14*:3:14, 290–296. <https://doi.org/10.1038/nmeth.4169>.
78. Tan, Y.Z., Baldwin, P.R., Davis, J.H., Williamson, J.R., Potter, C.S., Carragher, B., and Lyumkis, D. (2017). Addressing preferred specimen orientation in single-particle cryo-EM through tilting. *Nat. Methods* *14*, 793–796. <https://doi.org/10.1038/NMETH.4347>.
79. Pettersen, E.F., Goddard, T.D., Huang, C.C., Couch, G.S., Greenblatt, D.M., Meng, E.C., and Ferrin, T.E. (2004). UCSF Chimera—a visualization system for exploratory research and analysis. *J. Comput. Chem.* *25*, 1605–1612. <https://doi.org/10.1002/JCC.20084>.
80. Šali, A., and Blundell, T.L. (1993). Comparative protein modelling by satisfaction of spatial restraints. *J. Mol. Biol.* *234*, 779–815. <https://doi.org/10.1006/JMBI.1993.1626>.
81. Adams, P.D., Afonine, P.v., Bunkóczi, G., Chen, V.B., Davis, I.W., Echols, N., Headd, J.J., Hung, L.W., Kapral, G.J., Grosse-Kunstleve, R.W., et al. (2010). PHENIX: a comprehensive Python-based system for macromolecular structure solution. *Acta Crystallogr. D Biol. Crystallogr.* *66*, 213–221. <https://doi.org/10.1107/S0907444909052925>.
82. Emsley, P., and Cowtan, K. (2004). Coot: model-building tools for molecular graphics. *Acta Crystallogr. D Biol. Crystallogr.* *60*, 2126–2132. <https://doi.org/10.1107/S0907444904019158>.
83. Kidmose, R.T., Juhl, J., Nissen, P., Boesen, T., Karlens, J.L., and Pedersen, B.P. (2019). Namdinator - automatic molecular dynamics flexible fitting of structural models into cryo-EM and crystallography experimental maps. *IUCrJ* *6*, 526–531. <https://doi.org/10.1107/S2052252519007619>.
84. Croll, T.I. (2018). ISOLDE: a physically realistic environment for model building into low-resolution electron-density maps. *Acta Crystallogr. D Struct. Biol.* *74*, 519–530. <https://doi.org/10.1107/S2059798318002425>.
85. Chen, V.B., Arendall, W.B., Headd, J.J., Keedy, D.A., Immormino, R.M., Kapral, G.J., Murray, L.W., Richardson, J.S., and Richardson, D.C. (2010). MolProbity: all-atom structure validation for macromolecular crystallography. *Acta Crystallogr. D Biol. Crystallogr.* *66*, 12–21. <https://doi.org/10.1107/S0907444909042073>.
86. Sarkar, S., Witham, S., Zhang, J., Zhenirovskyy, M., Rocchia, W., and Alexov, E. (2013). DelPhi Web Server: A comprehensive online suite for electrostatic calculations of biological macromolecules and their complexes. *Commun. Comput. Phys.* *13*, 269–284. <https://doi.org/10.4208/CICP.300611.201011S>.
87. Stierand, K., Maaß, P.C., and Rarey, M. (2006). Molecular complexes at a glance: automated generation of two-dimensional complex diagrams. *Bioinformatics* *22*, 1710–1716. <https://doi.org/10.1093/BIOINFORMATICS/BTL150>.
88. Laskowski, R.A., and Swindells, M.B. (2011). LigPlot+: Multiple ligand-protein interaction diagrams for drug discovery. *J. Chem. Inf. Model.* *51*, 2778–2786. https://doi.org/10.1021/CI200227U/ASSET/IMAGES/LARGE/CI-2011-00227U_0005.JPEG.
89. Zhang, C., Shine, M., Pyle, A.M., and Zhang, Y. (2022). US-align: universal structure alignments of proteins, nucleic acids, and macromolecular complexes. *Nat. Methods* *19*, 1109–1115. <https://doi.org/10.1038/s41592-022-01585-1>.

STAR★METHODS

KEY RESOURCES TABLE

| REAGENT or RESOURCE | SOURCE | IDENTIFIER |
|---|---------------------|-------------------------------|
| Antibodies | | |
| StrepMAB-Classic HRP conjugate | IBA | Cat# 2-1509-001 |
| Recombinant Anti-Sodium Potassium ATPase antibody | abcam | Cat#ab76020; RRID: AB_1310695 |
| Goat Anti-Rabbit IgG H&L (HRP) | abcam | Cat# ab6721; RRID: AB_955447 |
| Bacterial and virus strains | | |
| MAX Efficiency™ DH10Bac Competent Cells | Gibco | Cat#10361012 |
| Chemicals, peptides, and recombinant proteins | | |
| Insect-Xpress | Lonza | Cat#BELN12-730Q |
| 10% Pluronic F-68 | Gibco | Cat#24040-032 |
| Gentamicin | Gibco | Cat#15750-037 |
| FreeStyle F17 | Gibco | Cat#A13835-01 |
| Fetal Bovine Serum | Sigma | Cat#F7524 |
| L-glutamine | Sigma | Cat#G7513 |
| Geneticin | Gibco | Cat#10131-027 |
| Penicillin-Streptomycin | Sigma | Cat#P4458 |
| Blasticidin | Sigma | Cat#SBR00022 |
| Doxycycline | Sigma | Cat#D3072 |
| Puromycin | Sigma | Cat#P9620 |
| Fugene | Promega | Cat#E2311 |
| cOmplete Protease Inhibitor Cocktail EDTA-free tablets | Roche | Cat#05056489001 |
| Phenylmethylsulfonylfluoride (PMSF) | Sigma | Cat#93482 |
| Deoxyribonuclease I from bovine pancreas | Sigma | Cat#DN25 |
| n-Dodecyl-beta-Maltoside (DDM) | Anatrace | Cat#D310 |
| Desthiobiotin | IBA | Cat#2-1000-002 |
| Brain Polar Lipid Extract | Avanti Polar Lipids | Cat#141101 |
| 16:0-18:1 PC (POPC) | Avanti Polar Lipids | Cat#850457 |
| Cholesteryl Hemisuccinate Tris Salt | Anatrace | Cat#CH210 |
| Prostaglandin E2 (PGE2) | Selleck Chemicals | Cat#S3003 |
| Topotecan (TPT) hydrochloride | Cayman Chemical | Cat#14129-50 |
| Methotrexate (MTX) | Bio Basic Inc | Cat# MB0612 |
| Adenosine 5'-monophosphate (AMP) sodium salt | Sigma | Cat#A1752 |
| Adenosine 5'-triphosphate (ATP) disodium salt, trihydrate | Bio Basic Inc | Cat#AB0020 |
| ATP-γ-S | Roche | Cat#11162306001 |
| Poly-L-ornithine hydrobromide | Sigma | Cat#P3655 |
| Critical commercial assays | | |
| ADP-Glo Kinase Assay | Promega | Cat#V6930 |
| Phosphate Assay Kit - PiColorLock | abcam | Cat#ab270004 |
| Cell Proliferation Kit I (MTT) | Roche | Cat#11465007001 |
| Deposited data | | |
| Cryo-EM map and model of IF MRP4 (no substrate added) | This paper | PDB: 8BJF; EMD: EMD-16088 |

(Continued on next page)

Continued

| REAGENT or RESOURCE | SOURCE | IDENTIFIER |
|---|---------------------------------|---|
| Cryo-EM map and model of OF MRP4 (TPT added) | This paper | PDB: 8BWO; EMDB: EMD-16292 |
| Cryo-EM map and model of IF MRP4 (MTX added) | This paper | PDB: 8BWP; EMDB: EMD-16293 |
| Cryo-EM map and model of IF MRP4 (TPT added) | This paper | PDB: 8BWQ; EMDB: EMD-16294 |
| Cryo-EM map and model of IF MRP4 (PGE2 added) | This paper | PDB: 8BWR; EMDB: EMD-16295 |
| Cryo-EM map of IF MRP4 in BPL+CHS nanodiscs (nothing added) | This paper | EMDB: EMD-16296 |
| Cryo-EM map of IF MRP4 in POPC nanodiscs (nothing added) | This paper | EMDB: EMD-16297 |
| Experimental models: Cell lines | | |
| Sf9 | Thermo Fisher | Cat#11496015 |
| HEK293-6E | Gift Yves Durocher | N/A |
| HEK293T LLP-Int-Blast | Matreyek et al. ⁷⁶ | N/A |
| Oligonucleotides | | |
| See Table S3 for primers used for mutagenesis | This paper | N/A |
| Recombinant DNA | | |
| ABCC4 cDNA ORF clone, Homo sapiens | GenScript | Accession# NM_005845.4; ClonID: OHu17173 |
| Plasmid: pNTL100 | This paper | N/A |
| Plasmid: pNTL240 (based on pNTL100, encoding ABCC4 cDNA ORF) | This paper | N/A |
| Plasmid: pNTL186 | This paper | N/A |
| Plasmid: pNTL260 (based on pNTL186, encoding ABCC4 cDNA ORF) | This paper | N/A |
| See Table S4 for additional plasmids encoding mutant variants of ABCC4 cDNA ORF | This paper | N/A |
| Software and algorithms | | |
| cryoSPARC | Punjani et al. ⁷⁷ | http://cryoSPARC.com |
| MODELLER | Šali and Blundell ⁸⁰ | https://sailab.org/modeller/ |
| Coot | Emsley and Cowtan ⁸² | https://www2.mrc-lmb.cam.ac.uk/personal/pemsley/cool/ |
| ISOLDE | Croll ⁸⁴ | https://isolde.cimr.cam.ac.uk |
| Namdinator | Kidmose et al. ⁸³ | https://namdinator.au.dk/ |
| PHENIX | Adams et al. ⁸¹ | https://www.phenix-online.org/ |
| MolProbity | Chen et al. ⁸⁵ | http://molprobity.biochem.duke.edu/ |
| Remote 3DFSC Processing Server | Tan et al. ⁷⁸ | https://3dfsc.salk.edu/ |
| PoseView | Stierand et al. ⁸⁷ | https://www.zbh.uni-hamburg.de/en/forschung/amd/server/poseview.html |
| LigPlot+ | Laskowski et al. ⁸⁸ | https://www.ebi.ac.uk/thornton-srv/software/LigPlus/ |
| UCSF Chimera | Pettersen et al. ⁷⁹ | https://www.cgl.ucsf.edu/chimera/ |
| DelPhi Web Server | Sarkar et al. ⁸⁶ | http://compbio.clemson.edu/sapp/delphi_webserver/ |
| US-align Online Web Server | Zhang et al. ⁸⁹ | https://zhanggroup.org/US-align/ |
| GraphPad Prism 9 | GraphPad Software | N/A |
| Illustrator | Adobe | N/A |
| BioRender.com | BioRender | https://biorender.com/ |
| Other | | |
| Grids Quantifoil R2/1 300 mesh Cu | Plano GmbH | Cat#S174-2 |

RESOURCE AVAILABILITY

Lead contact

Further information and requests for resources and reagents should be directed to and will be fulfilled by the Lead Contact, Nicholas M. I. Taylor (nicholas.taylor@cpr.ku.dk).

Materials availability

Plasmids generated in this study are available upon request from the [lead contact](#).

Data and code availability

- Atomic coordinates for IF MRP4 (no substrate added), OF MRP4 (TPT added), IF MRP4 (MTX added), IF MRP4 (TPT added), and IF MRP4 (PGE2 added) were deposited in the Protein DataBank under accession codes PDB: 8BJF, 8BWO, 8BWP, 8BWQ, and 8BWR, respectively.
- The corresponding electrostatic potential maps were deposited in the Electron Microscopy DataBank (EMDB) under accession codes EMD-16088, EMD-16292, EMD-16293, EMD-16294, and EMD-16295, respectively.
- The electrostatic potential maps for IF MRP4 in BPL+CHS nanodiscs (nothing added) and IF MRP4 in POPC nanodiscs (nothing added) were deposited in the EMDB under accession codes EMD-16296 and EMD-16297, respectively.
- All data reported in this paper will be shared by the [lead contact](#) upon request.
- This paper does not report original code.
- Any additional information required to reanalyze the data reported in this paper is available from the [lead contact](#) upon request.

EXPERIMENTAL MODEL AND STUDY PARTICIPANT DETAILS

Cell lines

Sf9 cells (used for generating baculovirus) were cultured in Insect-Xpress medium (Lonza, Cat#BELN12-730Q) supplemented with 0.1% pluronic acid (Gibco, Cat#24040-032) and 50 µg/mL gentamicin (Gibco, Cat#15750-037) at 27°C in suspension.

HEK293-6E cells (used for protein expression) were cultured in expression medium (FreeStyle F17 (Gibco, Cat#A13835-01)) supplemented with 1% FBS (Sigma, Cat#F7524), 4 mM L-glutamine (Sigma, Cat#G7513), 0.1% pluronic acid, and 50 µg/mL geneticin (Gibco, Cat#10131-027) at 37°C in suspension.

HEK293T cells (used for drug susceptibility assays) were cultured in plating medium (FreeStyle F17 supplemented with 10% FBS, 4 mM L-glutamine, 1x PenStrep (Sigma, Cat#P4458)), which was supplemented with either 100 µg/mL blasticidin (Sigma, Cat#SBR00022) (for non-transfected cells), 2 µg/mL doxycycline (Sigma, Cat#D3072) (for transfected cells), or 10 µg/mL puromycin (Sigma, Cat#P9620) (for transfected cells) at 37°C in adherent culture.

Frozen vials of the parental cell line (HEK293T LLP-Int-Blast), as well as protocols for maintaining and establishing derivative cell lines, were kindly supplied by Kenneth A. Matreyek (Case Western Reserve University). HEK293T LLP-Int-Blast cells were maintained in T-75 flasks and split every 48-72 h to a density of 10 M cells/plate.

METHOD DETAILS

Protein expression and purification

The cDNA encoding wildtype human MRP4 was obtained from GenScript (CloneID: OHu17173) and cloned into a donor plasmid based on the pHTBV1.1 vector⁷³ (pNTL100) to generate a construct featuring full-length MRP4 with a C-terminal HRV 3C-cleavable mVenus-tag linked in tandem to a Twin-Strep-tag and a 6xHis-tag (pNTL240). Mutant variants of MRP4 were generated by divergent PCR with the forward primer carrying the mutated codon. The construct was transformed into DH10Bac cells (Gibco, Cat#10361012) to generate recombinant bacmid (according to the manufacturer's protocol). Sf9 cells (Thermo Fisher, Cat#11496015) were transfected with purified bacmid to generate baculovirus-infected insect cells (BIICs): 50 µg purified bacmid was incubated for 30 min with 100 µg Fugene (Promega, Cat#E2311) in 1.5 mL complete Sf9 medium and added to 100 M Sf9 cells resuspended in 30 mL complete Sf9 medium. After 15 min at 27°C with no shaking, followed by 3 h at 27°C with 90 rpm shaking, the culture volume was expanded to 100 mL and incubated at 27°C with 120 rpm shaking for 96 h before the BIICs were harvested, aliquoted and frozen.

To generate first passage (P0) recombinant baculovirus, 21 M Sf9 cells were allowed to adhere in a T-75 flask for 30 min, the medium removed and replaced with 3 mL complete Sf9 medium containing 0.5 M resuspended BIICs. After 3 h at 27°C with no shaking, the culture volume was expanded to 11 mL, and the flask left for 96 h at 27°C with no shaking.

Subsequent passages of recombinant baculovirus were generated in suspension cultures: The P0 culture was harvested, centrifuged (1,500 rcf, 20 min) and 10 mL supernatant added to a 40 mL 2 M c/mL Sf9 culture, which was left for 72 h at 27°C with 120 rpm shaking to generate P1 baculovirus. The P2 culture was generated using the same supernatant:culture ratio and harvested by centrifugation.

The P2 baculovirus was precipitated by gently mixing P2 culture supernatant with a polyethylene glycol (PEG) solution (20% w/v PEG 10000, 1.2% NaCl) in a 4:1 v/v ratio and leaving it at 8°C with no shaking for >4 h in the dark. Precipitated baculovirus was

harvested by centrifugation (3,000 rcf, 45 min) and resuspended in PBS to 10% of the original supernatant volume to generate a 10x P2 baculovirus suspension.

For expression, the 10x P2 suspension was added at 1% v/v to 2 M c/mL HEK293-6E suspension cultures and the cultures left at 37°C with 150 rpm shaking for 72 h. The cells were harvested by centrifugation (500 rcf, 10 min), the pellets washed with PBS and centrifuged (1,500 rcf, 10 min) and flash frozen to be stored at -80°C.

For purification, the membrane fraction was isolated: Cells were resuspended in lysis buffer (100 mM HEPES pH 7.5, 200 mM NaCl, 10% glycerol) supplemented with EDTA-free Protease inhibitor cocktail (Roche, Cat#05056489001), 1 mM phenylmethylsulfonyl-fluoride (Sigma, Cat#93482), and 0.3 mg/mL DNase I (Sigma, Cat#DN25) and lysed on ice: ~35 mL aliquots were serially sonicated using nanoprobe. The lysate was cleared by centrifugation (8,000 rcf, 20 min, 4°C), and the membrane fraction isolated by ultracentrifugation (180,000 rcf, 45 min, 4°C) and resuspended at 0.2 g/mL in lysis buffer to be flash frozen.

Resuspended membranes were thawed and homogenized using a Dounce homogenizer, and n-Dodecyl-beta-Maltoside (DDM) (Anatrace, Cat#D310) added to a final concentration of 1% (w/v). After 30 min at 8°C with gentle agitation, insoluble material was pelleted by ultracentrifugation (100,000 rcf, 30 min, 4°C) and the decanted supernatant passed through a 0.22 µm filter.

The filtered supernatant was applied to a 1 mL StrepTrap HP column (GE, Cat#28-9075-47) equilibrated with binding buffer (100 mM HEPES pH 7.5, 150 mM NaCl, 0.03% DDM) and bound material eluted using elution buffer (100 mM HEPES pH 7.5, 150 mM NaCl, 0.03% DDM, 10 mM desthiobiotin (IBA, Cat#2-1000-002)). The peak elution fractions were pooled and incubated with HRV 3C protease (50 µg protease pr. 1 mg eluted protein) for 3 h at 8°C to cleave off the recombinant tag. The expression plasmid for HRV 3C protease (featuring an N-terminal 6xHis-tag) and protocols for expression and purification was kindly supplied by Jonathan Elegheert (then at University of Oxford).

Nanodisc reconstitution

To generate lipid nanodiscs, the HRV 3C digest was incubated with lipids and purified membrane scaffold protein (MSP1D1). Lipid stocks were prepared at ~10 mM (assuming average $M_w = 750$ Da for individual lipid molecules) by drying 10 mg lipids (either Brain Polar Lipid Extract (Avanti Polar Lipids, Cat#141101) for BPL+CHS nanodiscs or synthetic POPC (Avanti Polar Lipids, Cat#850457) for POPC nanodiscs) suspended in chloroform under N_2 , and resuspending the dry pellet in 200 µL 10% DDM, 660 µL 2x TS buffer (20 mM Tris pH 7.5, 150 mM NaCl), and 470 µL MQ to a final volume of 1330 µL. For the BPL stocks, the 10% DDM stock was supplemented with 2% CHS (Anatrace, Cat#CH210), which resulted in a final lipid:CHS molar ratio of ~60:40, which closely resembles the native lipid:cholesterol ratio in animal cell plasma membranes.⁷⁴ Lipids were resuspended by sonication.

The membrane scaffold protein, MSP1D1, was expressed and purified according to the protocol published by Bayburt et al.⁷⁵

HRV 3C digested WT hMRP4, purified MSP1D1 and resuspended lipids were mixed in a 1:10:250 M ratio: Protein and lipids were incubated for 1 h at 8°C with gentle agitation, after which MSP1D1 was added. After incubation for 5 min at 8°C with gentle agitation, 50 mg (wet weight) freshly prepared SM2-resin Bio-Beads (BioRad, Cat#1523920) were added to adsorb detergent, and the suspension incubated for 16 h at 8°C with gentle agitation.

After incubation, the Bio-Beads were allowed to settle, and the suspension removed and passed once through a 30 µm cut off disposable Micro Bio-Spin filter (Bio-Rad, Cat#7326204) to get rid of any remaining beads. The filtered sample was injected onto a Superose 6 Increase 10/300 GL gel filtration column (GE Healthcare) equilibrated in nanodisc buffer (20 mM HEPES pH 7.5, 150 mM NaCl) and fractions containing complete nanodiscs (Figure S1) pooled and concentrated using a Vivaspin 500 PES 50 kDa cut off spin filter (Sartorius, Cat#VS.0131).

ATPase activity assays

Two assays were used for detection of ATP hydrolysis: The ADP-Glo assay (Promega, Cat#V6930), which detects ADP, and the PiColorLock assay (abcam, Cat#ab270004), which detects orthophosphate (see Figure 2).

MTX interfered with the ADP-Glo assay (high luminescence counts were recorded even for the buffer controls). Consequently, the PiColorLock assay was used for samples containing MTX.

For both assays, three separate rounds of experiments were conducted (each with three technical replicates). Purified, nanodisc-reconstituted hMRP4 was resuspended in reaction buffer (20 mM Tris pH 7.5, 100 mM NaCl, 20 mM $MgCl_2$, 20 mM KCl) at 130 nM, and 100 µM PGE2 (Selleck Chemicals, Cat#S3003), 100 µM TPT (Cayman Chemical, Cat#14129-50) or 1 mM MTX (Bio Basic Inc, Cat# MB0612) was added where relevant and the sample preheated at 37°C for 2 min. To start the reaction, 100 µM nucleotides (either UltraPure ATP (from the ADP-Glo kit) or AMP (Sigma, Cat#A1752)) were added, and the reaction allowed to proceed for 30 min. For each assayed condition, equivalent samples featuring no protein (buffer controls) were included to allow for subtraction of background signal.

To quench the ADP-Glo experiments, ADP-Glo Reagent was added, followed by ADP-Glo Detection Reagent, and luminescence counts (proportional to the amount of ADP produced during the reaction) were recorded using a Fluoroskan Microplate Fluorometer.

To quench the PiColorLock experiments, freshly prepared PiColorLock Reagent Mix was added, followed by addition of stabilizer. Development of color (proportional to the amount of orthophosphate produced during the reaction) was followed by measuring A635 nm using a Fluoroskan Microplate Fluorometer.

Drug susceptibility assay

All cell lines used for this assay were based on the parental HEK293T LLP-Int-Blast cell line⁷⁶ featuring a synthetic landing pad at the AAVS1 locus. This landing pad encodes a Tet-promoter preceding a Bxb1 attP recombination sequence, followed by the Bxb1 recombinase gene linked with the BFP gene and a blasticidin resistance gene (*Bsd*) via parechovirus 2A-like translational stop-start sequences. The Tet-promoter allows for doxycycline inducible expression of Bxb1 recombinase (as well as BFP and *Bsd*) until it facilitates integration of a transfected Bxb1 attB-containing donor plasmid and thus terminates its own expression. The integrity of the landing pad is ensured by continuous blasticidin resistance selection.

To generate derivative cell lines (featuring doxycycline inducible overexpression of hMRP4 constructs), HEK293T LLP-Int-Blast cells were transfected with a modified version of the attB-PuroR-2A-mCherry donor plasmid⁷⁶ (pNTL186) in which the mCherry cassette has been replaced with the hMRP4 cDNA (encoding either wildtype or mutant protein) in tandem with an mVenus-tag linked in tandem to a Twin-Strep-tag and a 6xHis-tag (pNTL260). The fluorescent tag allows for verification of expression using fluorescence microscopy, while the Twin-Strep-tag allows for assessment of expression levels using Western blot.

Doxycycline dependent integration of the transfected donor plasmid (featuring the hMRP4 construct and the 2A-linked puromycin resistance gene) to generate the derivative HEK293T LLP-Puro-MRP4 cell line is verified by fluorescence microscopy and puromycin resistance selection.

To conduct the drug susceptibility assays, HEK293T LLP-Puro-MRP4 (encoding either wildtype or mutant recombinant hMRP4) and HEK293T LLP-Int-Blast (the parental cell line acting as negative control, NEG) were seeded in poly-L-ornithine (Sigma, Cat#P3655) coated 96-well plates at 40,000 cells/well (100 μ L volume) and incubated at 37°C for 24 h. Stocks of MTX (ranging from 0.005–0.5 mM) were generated from a 100 mM stock (in DMSO), 10x diluted (and pH-adjusted to pH 7.5) in PBS, and appropriately diluted in plating medium immediately prior to use (final [DMSO] < 0.5%).

To initiate MTX challenge, incubation medium was replaced with MTX-containing medium (100 μ L volume) and the plates incubated at 37°C for 4 h. To terminate MTX challenge, MTX-containing medium was removed, and each well washed with 2x100 μ L PBS before fresh plating medium (100 μ L volume) was added and the plates left at 37°C for 44 h.

Cell Proliferation Kit I (MTT) (Roche, Cat#11465007001) was used to assess cell viability 48 h post initiation of MTX challenge: Incubation medium was removed and replaced with plating medium (100 μ L volume) supplemented with 0.5 mg/mL MTT and the plates left at 37°C to allow for conversion of MTT into Formazan. After 2 h, 100 μ L detergent solution was added to each well and the plates left at 37°C for 22 h. To quantify cell viability, the A600 nm of each well was recorded using a Fluoroskan Microplate Fluorometer.

Electron microscopy sample preparation

All the samples used for cryo-EM were prepared using freshly purified and concentrated nanodisc-reconstituted hMRP4 and freshly prepared stocks of ATP (Bio Basic Inc, Cat#AB0020), ATP γ S (Roche, Cat#11162306001), MgCl₂, PGE2, TPT and MTX in stock buffer (100 mM HEPES pH 7.5, 150 mM NaCl).

For the sample used to obtain the reconstruction of IF MRP4 (no substrate added) in BPL+CHS nanodiscs (see Figures S2, S8A, and S9D), WT hMRP4 in BPL+CHS nanodiscs was incubated with 10 mM ATP γ S and 10 mM MgCl₂ for 30 min on ice prior to grid preparation.

For the sample used to obtain the (low resolution) reconstruction of IF MRP4 in POPC nanodiscs (nothing added) (see Figure S8B), WT hMRP4 in POPC nanodiscs was incubated for 30 min on ice prior to grid preparation.

For the sample used to obtain the additional reconstruction of IF MRP4 (nothing added) (see Figures S8C and S9E), a separate preparation of WT hMRP4 in BPL+CHS nanodiscs was incubated for 30 min on ice prior to grid preparation.

For the sample used to determine the structure of OF MRP4, E1202Q hMRP4 in POPC nanodiscs was incubated with 10 mM ATP, 10 mM MgCl₂, and 100 μ M TPT for 5 min at 37°C (to mimic turnover conditions) prior to grid preparation.

For the samples used to determine the structures of IF MRP4 (MTX or TPT added), WT hMRP4 in POPC nanodiscs was incubated with 10 mM ATP, 10 mM MgCl₂, and either 100 μ M MTX or 100 μ M TPT for 5 min at 37°C prior to grid preparation.

For the sample used to determine the structure of IF MRP4 (PGE2 added), WT hMRP4 in POPC nanodiscs was incubated with 1 mM PGE2 for 5 min at 37°C prior to grid preparation.

In all cases, sample was applied to a freshly glow discharged R2/1 Cu 300 Quantifoil grid (Plano GmbH, Cat#S174-2), and a Vitrobot Mark IV (FEI) was used to blot away excess sample and immediately plunge the grids into liquid ethane for vitrification of embedded sample.

Cryo-EM data collection and processing

Movies were acquired using a Titan Krios G2 (FEI) fitted with a Falcon 3EC detector operated in counting mode. Data acquisition was semi-automated using EPU (FEI, Thermo Scientific). Relevant details for the different datasets are summarized in Table S1 and S2.

The final reconstructions were obtained using cryoSPARC⁷⁷ as described in Figures S2–S6. Global and directional resolution of the final Coulomb potential maps was assessed using the Remote 3DFSC Processing Server⁷⁸ (<https://3dfsc.salk.edu/>). Local resolution of the final maps was calculated using cryoSPARC (using an FSC threshold of 0.143) and visualized using UCSF Chimera.⁷⁹ Euler angle distribution plots were generated using cryoSPARC.

MODEL BUILDING AND REFINEMENT

MODELLER⁸⁰ was used to generate a homology model of IF hMRP4 based on IF bMRP1 (PDB: 5UJ9), which was used as a starting point for model building of all four IF MRP4 atomic models. Likewise, a homology model of OF hMRP4 based on OF bMRP1 (PDB: 6BHU) was generated and used as a starting point for model building of the OF MRP4 structure. The homology models were rigid-body fit into the respective maps using UCSF Chimera⁷⁹ and real-space refined in PHENIX.⁸¹ The models were then inspected visually and manually fitted in Coot.⁸²

For further optimized fitting of the IF MRP4 structures, the online molecular dynamics pipeline, Namdinator,⁸³ was used. In all cases, the NBD1 moiety of the models could not be fitted reliably into the maps using this method. Consequently, NBD1 of the IF hMRP4 models was deleted and the remainder of the models fitted into the respective maps in UCSF Chimera. This was followed by fitting the respective NBD1 domains separately, while taking care of bond continuity for each of the complete models. Further fitting of amino acid side chains was done in iterative cycles of manual model building into the map using Coot and ISOLDE.⁸⁴

All ligands were fitted into map density in Coot and restraints generated in eLBOW (PHENIX), followed by real-space refinement of the complete models in PHENIX. MolProbity⁸⁵ was used to assess the quality of the final models. Maps and models were visualized using UCSF Chimera. The DelPhi Web Server⁸⁶ (http://compbio.clemson.edu/sapp/delphi_webserver/) was used for calculating the electrostatic energies (pH = 7.0, salt concentration = 0.15 M, default dielectric constant values) displayed in the electrostatic surface representation of IF hMRP4 (no substrate added) (visualized using UCSF Chimera).

Figure preparation

Figures were prepared using UCSF Chimera,⁷⁹ GraphPad Prism 9 (GraphPad Software), and Illustrator (Adobe). Elements of Figure 4 were obtained from BioRender.com. The US-align Online Web Server (<https://zhanggroup.org/US-align/>).

was used to generate the alignments shown in Figure S14.

QUANTIFICATION AND STATISTICAL ANALYSIS

For the ATPase activity assays, the data points represent the average values obtained from independent experiments (each with three technical replicates). Three rounds of independent experiments were performed for each condition.

For the drug susceptibility assay, separate estimates of pIC₅₀ for each cell line were obtained from nine rounds of independent experiments (each with six technical replicates), with each estimate obtained from fitting a non-linear sigmoidal dose-response model (using GraphPad Prism 9) to the data points from each experiment.

In order to phenotype the cell lines, a Šidák's multiple comparisons test was performed (using GraphPad Prism 9), comparing selected pairs of mean pIC₅₀ values: The mean pIC₅₀ values (the average of the independent estimates obtained from the fits displayed in Figure S11) of the individual cell lines were simultaneously compared to the mean pIC₅₀ values determined for the wild-type (WT) and parental (NEG) cell lines, that were chosen to represent the defining pIC₅₀ for, respectively, a resistant (R phenotype) cell line and a sensitive (S phenotype) cell line.

The results of the Šidák's multiple comparisons test are thus interpreted:

If the mean pIC₅₀ of a cell line is not significantly different from the mean pIC₅₀ of the WT cell line, but at the same time is significantly different from the mean pIC₅₀ of the NEG cell line, the cell line is said to display an R phenotype.

If the mean pIC₅₀ of a cell line is significantly different from the mean pIC₅₀ of the WT cell line, but at the same time is not significantly different from the mean pIC₅₀ of the NEG cell line, the cell line is said to display an S phenotype.

If the mean pIC₅₀ of a cell line is significantly different from the mean pIC₅₀ of the WT cell line, and at the same time is significantly different from the mean pIC₅₀ of the NEG cell line, and falls within the interval between these two estimates, the cell line is said to display an intermediate (I) phenotype.